Article

Rational Design of In Vivo Tau Tangle-Selective Near Infrared Fluorophores: Expanding the BODIPY Universe

Peter Verwilst, Hye-Ri Kim, Jinho Seo, Nak-Won Sohn, Seung-Yun Cha, Yeongmin Kim, Sungho Maeng, Jung-Won Shin, Jong Hwan Kwak, Chulhun Kang, and Jong Seung Kim

J. Am. Chem. Soc., **Just Accepted Manuscript** • DOI: 10.1021/jacs.7b05878 • Publication Date (Web): 31 Aug 2017

Rational Design of In Vivo Tau Tangle-Selective Near Infrared Fluorophores: Expanding the BODIPY Universe

Peter Verwilst,[†‡] Hye-Ri Kim,[§‡] Jinho Seo,[†] Nak-Won Sohn,[§] Seung-Yun Cha,[§] Yeongmin Kim,[§] Sungho Maeng,[§] Jung-Won Shin,[§*] Jong Hwan Kwak,[Δ*] Chulhun Kang,[§*] Jong Seung Kim[†*]

[†] Department of Chemistry, Korea University, Seoul 02841, Korea
[§] School of East–West Medical Science, Kyung Hee University, Yongin 17104, Korea
[Δ] School of Pharmacy, Sungkyunkwan University, Suwon 16419, Korea

ABSTRACT: The elucidation of the cause of Alzheimer's disease remains one of the greatest questions in neurodegenerative research. The lack of highly reliable low-cost sensors to study the structural changes in key proteins during the progression of the disease is a contributing factor to this lack of insight. In the current work, we describe the rational design and synthesis of two fluorescent BODIPY based probes, named **Tau 1** and **Tau 2**. The probes were evaluated on the molecular surface formed by a fibril of the PHF6 (^{306}VQIVYK^{311}) tau fragment using molecular docking studies to provide a potential molecular model to rationalize the selectivity of the new probes as compared to a homologous Aβ selective probe. The probes were synthesized in a few steps from commercially available starting products and could thus prove to be highly cost effective. We demonstrated the excellent photophysical properties of the dyes, such as a large Stokes' shift and emission in the near infrared (NIR) window of the electromagnetic spectrum. The probes demonstrated a high selectivity for self-assembled microtubule associated protein tau (MAPT, Tau protein), both in solution and cell-based experiments. Moreover, the administration to an acute murine model of tauopathy clearly revealed the staining of self-assembled hyperphosphorylated tau protein in pathologically relevant hippocampal brain regions. **Tau 1** demonstrated efficient BBB penetrability, and demonstrated a clear selectivity for tau tangles over Aβ plaques, as well as the capacity for *in vivo* imaging in a transgenic mouse model. The current work could open up avenues for the cost-effective monitoring of the tau protein aggregation state in animal models as well as tissue staining. Furthermore, these fluorophores could serve as the basis for the development of clinically relevant sensors, for example based on PET imaging.

INTRODUCTION

Intraneuronal neurofibrilary tangles (NFT), consist of paired helical filaments, comprising the hyperphosphorylated microtubule associated protein tau (MAPT, tau protein)[1] and, together with extracellular deposits of β amyloid (Aβ) protein, are classical hallmark features observed in the brains of Alzheimer's patients.[2] Furthermore NFTs are a prevalent feature of other neurodegenerative diseases, such as Down syndrome, amyotrophic lateral sclerosis (ALS), Pick's disease, Parkinson's disease and some forms of familial dementia, collectively known as tauopathies.[3] Importantly, the NFT burden has a strong correlation to the disease progression and severity,[4] unlike Aβ in AD. Considering the potential applicability in other tauopathies, the development of tau based imaging probes is of paramount importance.

In humans, tau proteins exist in six isoforms, ranging from 352 to 441 amino acids in length, with no clearly defined secondary structure.[3,5] The association of these proteins with microtubules in the axonal compartment of neurons, through predominantly electrostatic interactions, promotes microtubule growth and stability.[3,5-7] Extensive post-translational modifications, such as phosphorylation of serine and threonine residues, methylation, acylation, glycation and truncation have been observed.[8-10] Whereas the dynamic phosphorylation and dephosphorylation of tau proteins is an important feature in healthy individuals, the disruption of this delicate balance in favor of hyperphosphorylated tau proteins triggers a pathological response. As a result of diminished electrostatic interactions, tau proteins disassemble from microtubules and are missorted to the somatodendritic compartment, where they self-aggregate, resulting in intracellular accumulation of NFTs.[11,12]

The structure of self-aggregated tau proteins is hypothesized to consist of a core of parallel beta sheets, surrounded by a fussy coat of less structured polyelectrolyte brushes.[13] However, no definite structure based on NMR or X-ray crystallography is available, making the discovery of tau tangle specific beta sheet binders a laborious task.

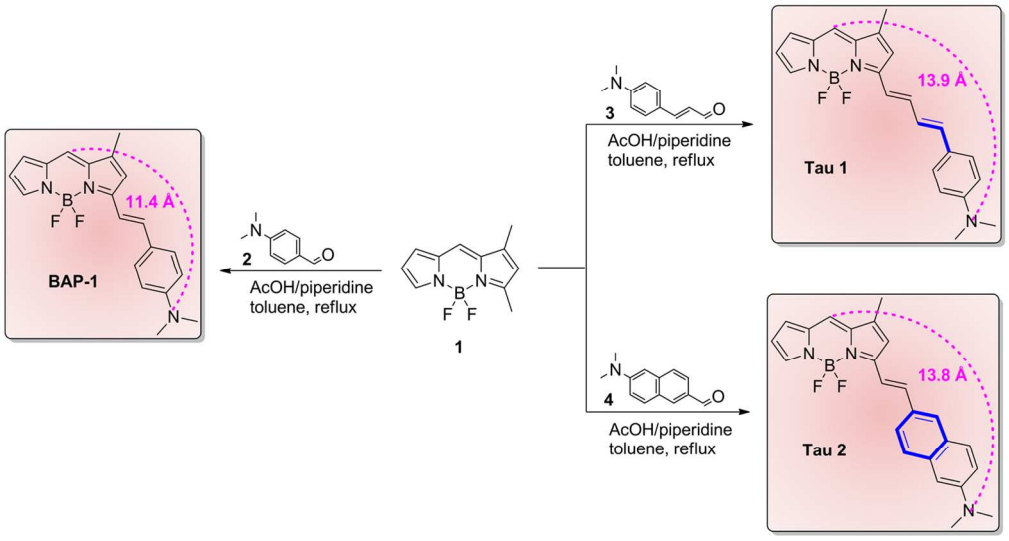

Scheme 1. Synthetic approach towards **BAP-1** and **Tau 1-2**. The structural modifications relative to **BAP-1** are marked in blue. The *N* – BODIPY *C*8 (*meso*) distance, as determined from the optimized structure by DFT is shown in magenta (See SI for DFT calculation details).

Hence, no clear pharmacophore model has been identified thus far.[14] In recent years two hypotheses guiding the design of NFT binders have emerged. Firstly, it was discovered from a series of benzothiazole-containing donor-acceptor dyes that a distance of 13 to 19 Å between the donor and acceptor parts benefits NFT selectivity, whereas shorter distances favor Aβ plaques.[15] Secondly, amongst similar compounds, those containing fused ring systems frequently have an increased selectivity for tau tangles over Aβ fibrils.[14]

Hitherto only very few NIR (near infrared) emissive fluorescent probes for NFTs have been discovered, either recognizing specific phosphorylation patterns,[16] or beta sheet binders exhibiting a certain degree of selectivity.[15,17] In the current work, we discuss two rationally designed BODIPY (4,4-difluoro-4-bora-3a,4a-diaza-*s*- indacene) based probes, aptly named **Tau 1** and **Tau 2**, resulting from the elongation of conjugation and annulation of a known Aβ plaque binding dye, known as **BAP-1**[18] (Scheme 1), in order to investigate the scope and the potential translation of the above mentioned design hypotheses to this structurally unrelated class of dyes. The BODIPY fluorophore was chosen owing to its excellent photophysical properties such as high molecular extinction coefficients, quantum yields and photostability, combined with attractive, often orthogonal chemical modifications.[19,20]

RESULTS AND DISCUSSION

Synthesis. BAP-1 and **Tau 1-3** were synthesized from the common precursor BODIPY **1** *via* Knoevenagel condensations with their corresponding aldehydes (**2-4**) (Scheme 1). The characterization of all new final products by ^{1}H and ^{13}C NMR, as well as ESI-MS can be found in the SI (Figures S1-S6).

Fluorescence and theoretical calculations. The photophysical characteristics of the dyes were determined in relation to the environmental properties of various solvents (Table S1). As can clearly be seen from Figures S7-S9, **BAP-1**, **Tau1** and **Tau2** exhibit very similar behavior, showing increased Stokes' shifts and decreased fluorescence quantum yield in relation to the solvent polarity (as quantified by the solvent dielectric constant). None of the dyes showed a dependence on the solvent viscosity. Particularly the Stokes' shift's dependence on the dielectric constant, as well as their relatively large value in relation to the very small Stokes' shifts commonly observed in BODIPY-type dyes (in the range of 10 nm), indicates the presence of intramolecular charge transfer (ICT) upon excitation.

The dependency of the peak wavelength of absorbance and emission of the fluorophores were studied in relation to the solvent polarity, using a scale for the polarity that treats the polarizability (induced dipole) and the dipolari-

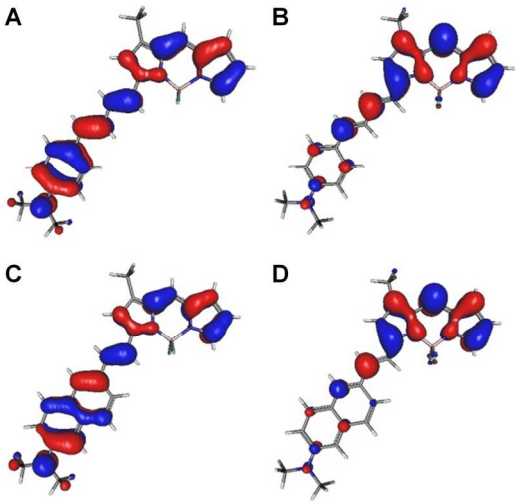

Figure 1. Calculated frontier orbitals of **Tau 1** and **Tau 2** by density functional theory using B3LYP at the 6-311++G** level of theory. (a-b) HOMO and LUMO orbital of **Tau 1**. (c-d) HOMO and LUMO orbital of **Tau 2**. Electron densities are displayed at the 0.03 e·bohr^{-3} isodensity surface.

ty (permanent dipole) independently, as described by Catalán.[21] The maximum absorbance wavelength correlated well with the solvent polarizability in all fluorophores (Figure S10), as a result of the solvent electronic stabilization of the Franck-Codon state, whereas the maximum emission wavelength corresponded well with the solvent dipolarity, *via* the solvent cage rearrangement after the geometrical relaxation of the excited state molecule in **Tau 1-2** (Figure S11). Taken together these solvatochromic effects clearly point to an excited state that has a significantly higher dipole moment than the ground state, which is a key characteristic of fluorophores exhibiting ICT in the excited state.

The energy levels of the dyes' molecular orbitals in vacuum were calculated by B3LYP DFT calculations at the 6-311++G** level of theory (Figure 1 and Table S2). The electron distributions in the frontier orbitals revealed an electron redistribution from the aniline or aminonaphthalene pendants in the highest occupied orbital (HOMO) to the BODIPY core in the lowest unoccupied orbital (LUMO) (Table S2), thus confirming the involvement of an ICT process as a rationale for the observed large Stokes' shifts.

The spectra of **BAP-1** and **Tau 1-2** in acidified chloroform resulted in significantly hypsochromic shifts in both the absorption and emission spectra (Figure S12), as compared with those in non-acidified chloroform (Figure S13), with associated Stokes' shifts of classical BODIPY dyes (around 6 nm). These results further demonstrate the involvement of ICT, as the protonation of the pendant aniline moieties disrupts the charge transfer process.

Unlike many other probes detecting cross beta sheet protein morphologies, **BAP-1**, as well as **Tau 1-2**, did not show a fluorescence quantum yield dependence on the solvent viscosity and did thus not function as a molecular rotor, despite their structural resemblance. The selective recognition of tau protein cross beta sheets, combined with the relatively apolar nature of the beta sheet structures of self-assembled tau protein, should thus ensure increased fluorescence upon binding, whereas the ICT-based large Stokes' shifts are greatly beneficial to imaging applications, preventing the re-absorbance of emitted light often encountered in dyes with small Stokes' shifts, thus resulting in better signal over noise ratios.

Finally, the photostability of the dyes was determined *versus* Rose Bengal in DMF. As can be seen in Figure S14, all dyes exhibited a similar resistance to photobleaching under the employed conditions with a stability of 2.43 ± 0.04, 2.42 ± 0.07 and 2.59 ± 0.06 -fold the stability of Rose Bengal for **BAP-1**, **Tau 1** and **Tau 2**, respectively.

Molecular docking studies. The interactions of **BAP-1** and **Tau 1-2** with a crystal structure of the PHF6 fragment (^{306}VQIVYK^{311}) of the R3 microtubule binding region of tau protein were evaluated using molecular docking studies. The PFH6 sequence has been demonstrated to play a pivotal role in the propensity of tau protein to form self-assembled structures and was identified as responsible for the nucleation of the tau protein,[22,23] and has as such been studied extensively in the quest for ligands to prevent the nucleation event as a potential therapeutic for tauopathies.[24-26] In particular, the interaction between adjacent stacks of parallel layers of ^{306}V and ^{308}I have been identified as a target to prevent the initiation of protein nucleation.[25] The crystal structures of this hexapeptide consist of a steric zipper architecture, and co-crystallization with various compounds reveals a propensity to generate tunnels along the fibril axis, either naturally or induced by co-crystallization with small organic ligands.[27-30] A significant degree of polymorphism exists, with crystal structures demonstrating 0 (PDB: 2ON9),[27] 1 (PDB: 3OVL)[28] or 2 (4NP8 and 5K7N)[29,30] tunnels along the fibril axis. The structure of tunnels induced by co-crystallization with cross-beta sheet binders DDNP and curcumin (1 tunnel) are also highly conserved in the structures exhibiting two tunnels.

Firstly, the interactions of **BAP-1** and **Tau 1-2** were studied on a 6-mer fibril built from the axis elongation of a single VQIVYK peptide extracted from a recent 1.1Å resolution crystal structure (PDB: 5K7N).[30] The docking studies revealed a predominant interaction with the surface formed by the QVK along the fibril axis, with the affinity in the order of **BAP-1** < **Tau 1** < **Tau2** (data not shown). Importantly, the probes did not show a strong affinity for the opposite surface of the protein, including the ^{306}V and ^{308}I believed to be important for tau aggregation inhibition.

Subsequently, a 6-mer model of the most conserved channel, formed by four adjacent beta sheet structures was constructed (Figure S15). The tunnel exhibits a combination of hydrophobic surfaces, as well as some hydrophilic surfaces by in-plane and stacked hydrogen bonding. The interactions of **BAP-1** and **Tau 1-2** in the tunnel cavity were assessed, alongside the structures of the two previously described NIR emissive cross beta sheet-binding tau probes **3h**[17] and **PBB5**[15] (Table S3). Fascinatingly, **Tau 1-2** as well as **3h** and **PBB5** demonstrated a tight fit in the tunnel as shown in Figure 2 and S16-S17, respectively, with **BAP-1** showing a significantly lower calculated binding affinity (Table S3), which can be rationalized by a smaller surface area and thus a smaller amount of surface interactions.

In order to test the generality of the docking study, the calculations were repeated with 12 lead compounds in the design of tau selective PET probes, identified from vast libraries of compounds (Table S3, Figures S19-S31). With the exception of two compounds (**F-ATPZ-38** and **Astemizole**; see Table S3, entries 1 and 3 respectively), all probes demonstrated calculated affinities in the same range or higher than **Tau 1-2**, **3h** and **PBB5**. As judged from their structures, neither **F-ATPZ-38** nor **Astemizole** are likely to act as cross-beta sheet binders, but are rather expected to interact with a different topology on the hyperphosphorylated Tau protein aggregates.

In view of these results, we postulate that this tunnel architecture along the fibril axis may be a major binding site of cross-beta sheet binding probes with hyperphosphorylated tau protein.

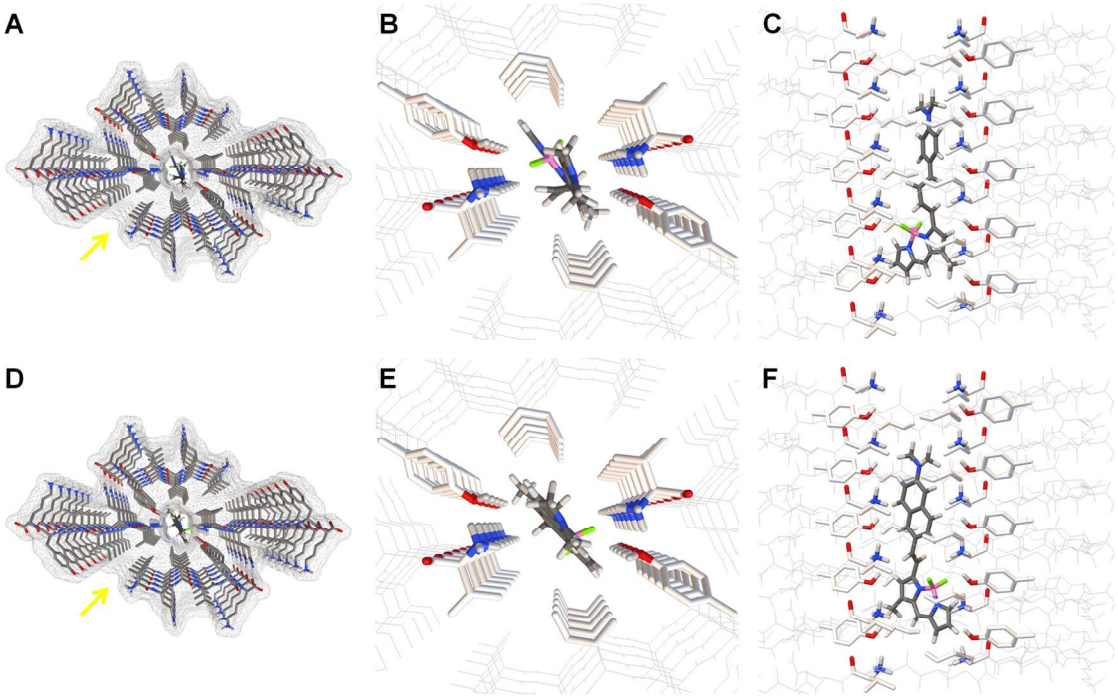

Figure 2. Molecular docking of **Tau 1** (A-C) and **Tau 2** (D-F). A and D) Top view of the molecule docked in the tunnel formed by 4 adjacent stacked beta sheets, protein molecular surface depicted. B and E) zoomed top view of the tunnel, side chains comprising the tunnel are depicted as sticks, others as lines. C and F) Side view of the molecule in the in the protein tunnel, side chains comprising the tunnel are depicted as sticks, others as lines. The yellow arrow indicates the viewing direction for panels C and F.

The results of this theoretical study need to be interpreted with some level of caution however, as the complex structure of self-assembled tau protein precludes the definite pinpointing of cavities formed by self-aggregating PHF6 protein as a potential, or even predominant, binding location.

Nevertheless these results in the protein cavities could potentially provide a molecular insight and rationale for the improved binding affinities observed in longer probes with tau tangles *vs.* Aβ plaques,[15] and could prove useful for the design of novel (fluorescent) probes for tau aggregates.

Tau 1 and Tau 2 selectively interact with Tau protein aggregates in solution. The emission spectra of a sample of **Tau 1-2**, alongside **BAP-1** and the universal beta sheet fluorophore thioflavin T (**ThT**)[31] as the controls, were monitored over time to analyze the probes' selectivity for tau protein aggregates over beta amyloid aggregates (Figures 3 and S32). As evident from Figure 3A-B, tau protein aggregation was induced by incubation with the polyanionic heparin,[32] and a clear time-dependent fluorescent enhancement could be observed in the presence of both **Tau 1** and **Tau 2**. The maximum fluorescence increase (6.4-fold and 9.3-fold for **Tau 1** and **Tau 2**, respectively) was reached after 48 hour heparin incubation. However, no significant fluorescence could be observed in the presence of heparin alone (Figure 3A-B). By contrast, **Tau 1** and **Tau 2** both show only trivial responses to the presence of beta amyloid solutions (Figure 3C-D). These data suggest that **Tau 1** and **Tau 2** are highly selective to Tau protein aggregates over Aβ aggregates. **ThT** and **BAP-1** demonstrated a strong fluorescent response to both of tau and Aβ amyloid aggregation assays (Figure S32).

In order to determine the influence of the dyes on the aggregation behavior of tau derived peptides, an aggregation inhibiting assay was performed on the AcPHF6 peptide. The assays showed that the aggregation of the peptide, as recorded by the time dependent fluorescence of **ThT**, was not affected by the presence of **BAP-1** or **Tau 1** at the concentrations used in the current work (Figure S33), as the time to reach maximum fluorescence was not significantly different. The maximum fluorescence intensity of **ThT** was reduced upon the addition of the dyes, suggesting a competition for binding sites on the peptide aggregates with **BAP-1** and **Tau 1**. The influence of **Tau 2** was not determined as the solubility in the high buffer strength medium was suboptimal for this dye.

The fluorescence of **BAP-1** and **Tau 1** in the NIR region did also increase under these conditions, with similar fluorescence rise times, providing extra evidence for a binding interaction with the AcPHF6 peptide (Figure S34), thus validating the results of the docking studies.

Cytotoxicity of Tau 1 and Tau 2. Prior to assessing the specificity of the probes in a cellular environment, the cytotoxicity of the probe was assessed using an MTT assay in a number of brain-derived cell lines: SKNMC (Human neuroblastoma), U87 (Human glioblastoma), SH-SY5Y (Human neuroblastoma), C6 (Rat brain glioma), N2A (Mouse brain neuroblastoma) as well as a human primary brain neuron culture. No significant toxicity was observed

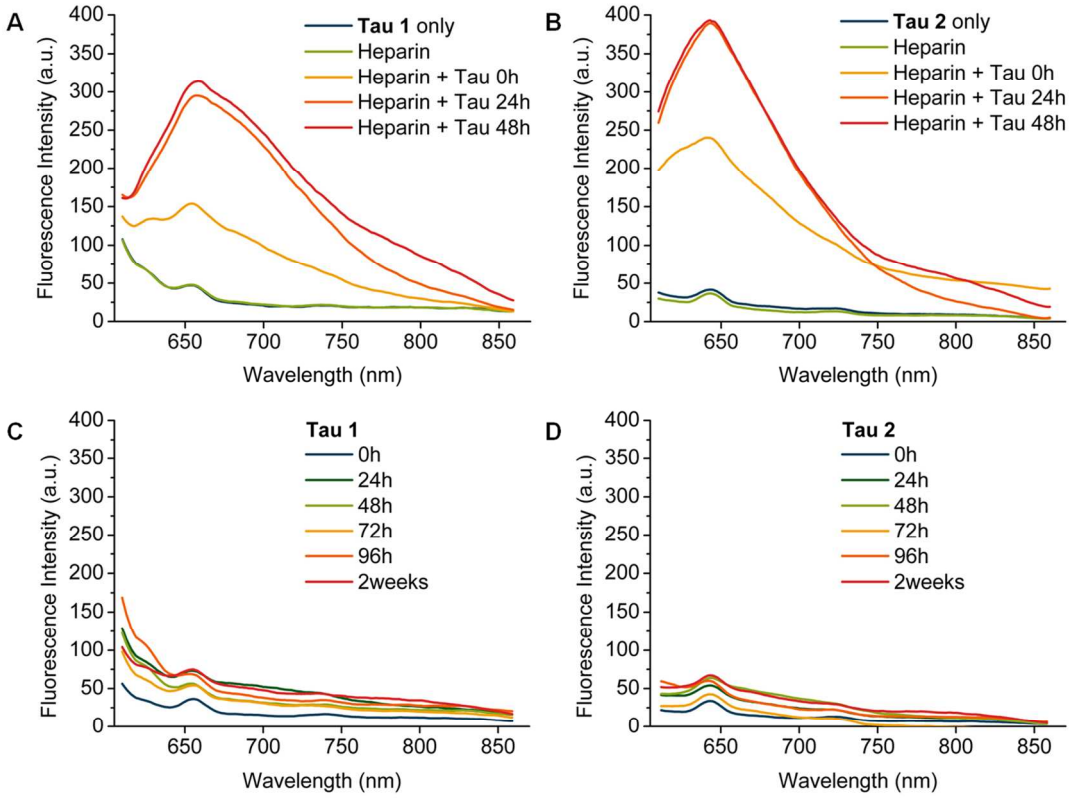

Figure 3. Time dependent fluorescence enhancement of **Tau 1-2** (10 μM) in the presence of protein aggregates. (a) Emission spectra of **Tau 1** in the presence of tau protein (10 μM) and heparin (2.5 μM), excited at 590 nm, (b) Emission spectra of **Tau 1** in the presence of tau protein (10 μM) and heparin (2.5 μM), excited at 580 nm, (C-D) Emission spectra of **Tau 1-2** in the presence of Aβ fibrils (50 μM).

at concentrations as high as 10 μM in any of these cells after 48 hours of incubation (Figure S35).

Tau 1 and Tau 2 selectively visualize okadaic acid-induced tau hyperphosphorylation in cells. Human neuroblastoma SH-SY5 cells treated with okadaic acid (OA),[33] a potent inhibitor of a broad range of serine/threonine phosphatases, is a well-known cell culture model for *in vitro* tau hyperphosphorylation, and the tau phosphorylation pattern is similar to that obtained from human AD brain tissue.[34] As shown in Figure S36, the addition of 50 nM OA to SH-SY5 cells clearly resulted in a time-dependent increase tau protein expression and its hyperphosphorylation.

Having confirmed the hyperphosphorylation in the cell model, **Tau 1-2**, **BAP1** or **ThT** (500 nM each) were added to SH-SY5 cells incubated with 100 nM OA for 6 hours, and the fluorescent images were quantitatively analyzed. As seen in Figure 4A and B, all probes demonstrated an increase in the fluorescence intensity as compared to cells not pre-incubated with OA. Whereas an increase in fluorescence of 4.41 ± 1.53 and 2.92 ± 1.10 fold was observed for **Tau 1** and **Tau 2,** respectively, **BAP1** and **ThT** showed a less pronounced effect with fluorescence enhancements (1.71 ± 0.35 and2.17 ± 0.45 fold, respectively). Thus, these results clearly indicate **Tau 1** and **Tau 2**'s preference for tau protein aggregates.

To characterize the fluorophores' response to Aβ, a possible cause of interference in the selective visualization of tau aggregates in brain tissues, their fluorescent responses were investigated in SH-SY5Y cells pretreated with freshly dissolved $A\beta_{1\text{-}42}$ peptide (50 μg/mL) for 48 hours,[35,36] the formation of intracellular amyloid fibrils was confirmed by Western Blot analysis of cell lysates (Figure S37).

As can be seen in Figure 4C-D, **Tau 1** and **Tau 2** show little fluorescence enhancement in the Aβ-treated cells, compared to untreated cells, whereas **BAP-1** and **ThT** did reveal a small but significant increase in the fluorescence intensity (1.57 ± 0.42 and 2.35 ± 0.61-fold, respectively). These results clearly demonstrate that **Tau 1** and **Tau 2** are capable of detecting hyperphosphorylated tau protein aggregates even in cellular environments without any significant interference by Aβ aggregates.

Tau 1 visualizes tau hyperphosphorylation in an acute murine model for tauopathies in aged mice. Encouraged by the previous results of **Tau 1**'s selectivity to hyperphosphorylated tau aggregates in cells, its application to an *in vivo* animal model of tauopathy was attempted. For a relevant animal model, aged mice (23 months) were subjected to a single injection of 10 ng of OA to the lateral amygdala in brain to induce tau hyperphosphorylation and its aggregation in the region of the hippocampus.[37] The CA1 and CA3 regions are particularly interesting since these regions are among the early

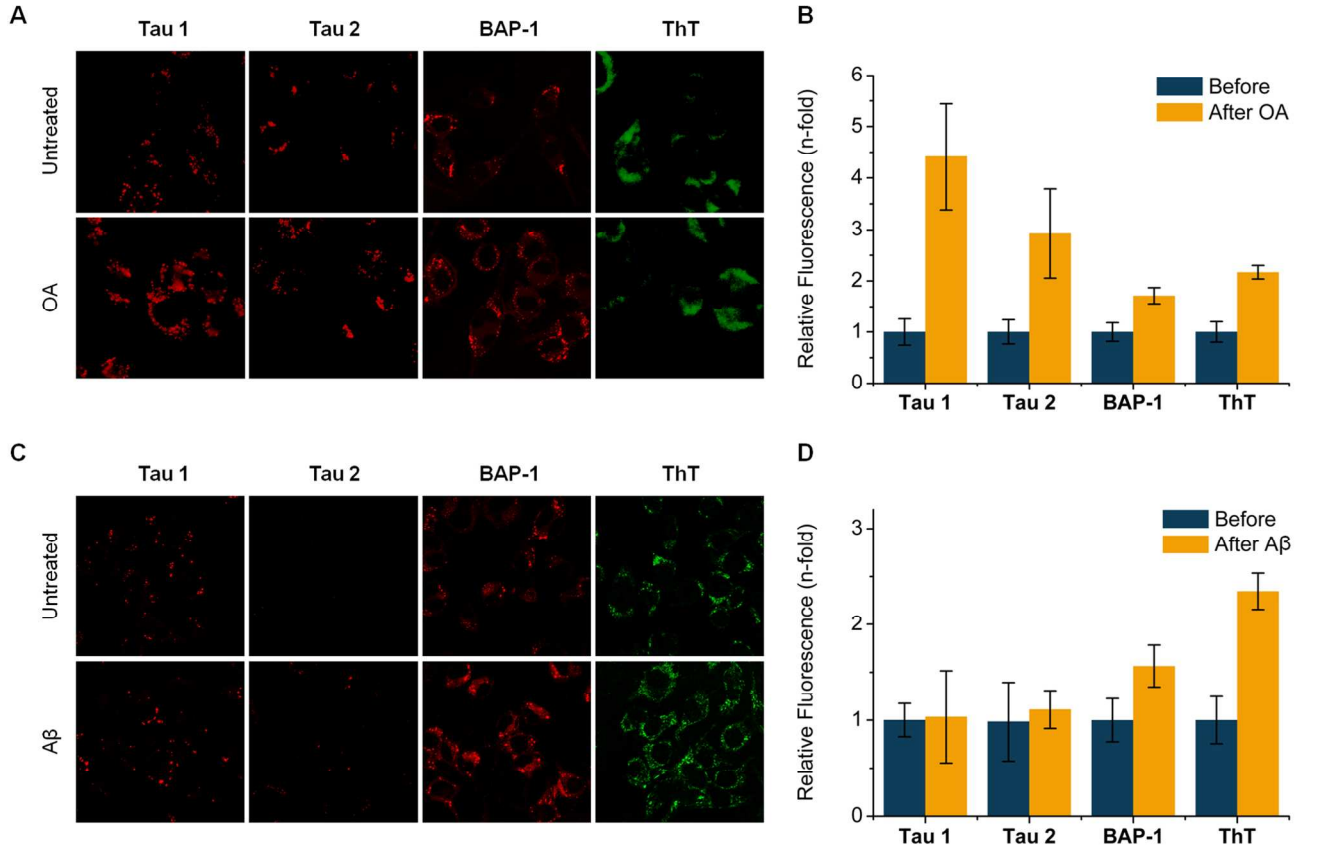

Figure 4. (a) Fluorescence images of SH-SY5Y cells incubated with **Tau 1**, **Tau 2**, **BAP-1** and **ThT** (500 nM) for 20 min at 37°C. Top: Untreated cells, Bottom: pre-incubated with okadaic acid (100 nM) for 6hr. **ThT** was excited at 458 nm and the emission was recorded using a 475-525 nm band pass filter. **Tau 1-2** and **BAP-1** were excited at 633 nm and the fluorescence was collected at wavelengths higher than 650 nm. (b) Florescence intensity per cell relative to untreated cells (n=5), as determined using image J.[38] Error bars designate standard deviation. (c) Fluorescence images of SH-SY5Y cells using amyloid beta peptide with **Tau 1**, **Tau 2**, **BAP-1** and **ThT**. After treatment of amyloid beta peptide (50 μg/mL) for 48 hr, the probes (1 μM) were incubation for 15 min at 37°C (bottom). Untreated cells were incubated with the probes for 15 min without peptide (top). **ThT** was excited at 458 nm and the emission was recorded using a 475-525 nm band pass filter, **Tau 1-2** and **BAP-1** were excited at 633 nm and the fluorescence was collected at wavelengths higher than 650 nm. (d) Fluorescence intensity per cell relative to untreated cells (n=5), as determined using image J.[38] Error bars designate standard deviation.

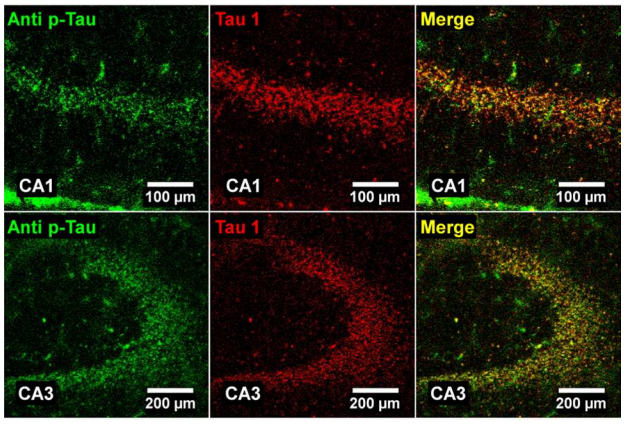

Figure 5. Confocal imaging of the CA1 (Top) and CA3 (Bottom) hippocampal regions of OA treated mice. Dual staining with the hyperphosphorylated tau protein antibody (AT-180) and **Tau 1** reveals a very high degree of overlap. The fluorescence image of **Tau 1** was collected using excitation at 633 obtained using excitation at 488 nm with a 505-550 nm bandpass filter.

regions to be affected by tau protein hyperphosphorylation and intraneuronal neurofibrilary tangles deposition in the course of disease progression in models[37] and human patients.[39] Indeed, *ex vivo* analysis of the hippocampal regions of the mouse brain, resulted in distinct staining of bands in the CA1 and CA3 region of the brain, corresponding to the pyramidal neuronal somatodendritic compartments (Figure S38) where, on the brain slice from mice without OA, **Tau 1** showed virtually no fluorescence under the same imaging settings.

In order to pursue whether the tau-positive regions in the brain slice are the locations for the hyperphospory-lated tau aggregates or not, a confocal microscopy study of the emission from **Tau 1** and an antibody against hyperphosphorylated tau protein was conducted. The images in Figure 5 show that, in CA1 and CA3 hippocampal regions of the OA-treated mice, **Tau 1** demonstrates intense fluorescence spots and, as anticipated the cell bodies in these regions are clearly overlapped with the fluorescence of the antibody. At the scale of an individual

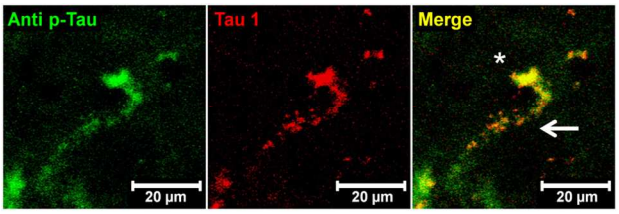

Figure 6. Confocal imaging of a single hippocampal neuron of an OA treated mouse. Dual staining with the hyperphosphorylated tau protein antibody AT-180 and **Tau 1** demonstrates significant amounts of tau missorting to the somatodendritic compartment (*) of the neuron, as well as sporadic hyperphosphorylated tau deposits along the axon (arrow). The fluorescence image of **Tau 1** was collected using excitation at 633 nm with a 650 nm longpass filter and that of AT180 was obtained using excitation at 488 nm with a 505-550 nm bandpass filter.

neuron, some revealed a flame-like feature as shown in Figure 6. This feature can be interpreted as tau protein aggregates sorted to the somatodendritic compartment of the neuron as well as along the axon, to a lesser extent. Although hyper-phosphorylated tau aggregates were mainly found in axonal stem of neurons in human patients, its somatic localization was often observed in animal models of tau hyperphosphorylation (Figure 6).[12] Nonetheless, the results in Figures 5 and 6 demonstrate **Tau 1**'s capability as selective fluorescent sensor, responsive to hyperphosphorylated tau aggregates in brain tissues. Co-localization experiments with a fluorescent antibody for $A\beta_{1-42}$ showed only faint, mostly non-specific fluorescence, thus confirming the fluorescence originating for **Tau 1** in OA-treated mice did not result from $A\beta_{1-42}$ staining (Figure S39).

The **Tau 1** fluorescence dependence on the tau protein burden in the OA-treated mouse model was further validated, as 10-week old OA-treated mice demonstrated only very faint fluorescence of **Tau 1** (Figure S40), in accordance with the reported age-dependent reduction of the PP2A (protein phosphatase 2A) expression levels,[40] with PP2A being the most important phosphatase maintaining tau protein in its non-phosphorylated form,[41] as well as being a prime target for OA inhibition.[42] Thus the effect of OA treatment on tau hyperphosphorylation would be expected to be more severe in aged mice.

Blood-brain barrier penetrability of Tau 1. In order to assess the BBB penetrability of **Tau 1** in mice, the dye was injected via the tail vein and the animals were sacrificed after one hour. The brain was cryosectioned and imaging of **Tau 1** demonstrated fluorescence originating from the pyramidal neurons in the hippocampus (Figure S41). Whereas a mouse injected with the vehicle only failed to show any fluorescence. These results clearly indicate the potential of **Tau 1** to cross the blood-brain barrier.

Tau 1 shows selectivity of Tau aggregates over Aβ plaques in a transgenic mouse model of AD. Tau tangle selectivity was assessed using the 3xTg mouse model of AD.[43] This triple transgenic model expresses both the Swedish (KM670/671NL) mutation of the human amyloid

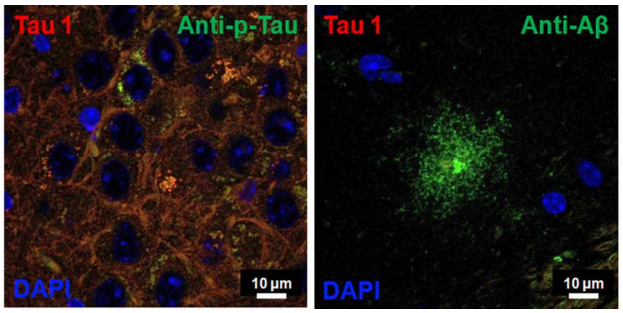

Figure 7. Merged confocal imaging of hippocampal regions of 3xTg mice. Left: Dual staining with the hyperphosphorylated tau protein antibody AT180 and **Tau 1**; Right: Dual staining with the amyloid beta antibody 6e10 and **Tau 1**. The fluorescent image of **Tau 1** was obtained using excitation at 633 nm with a 650 nm longpass filter and AT180 and 6e10 were obtained using excitation at 488 nm with a 505-550 nm bandpass filter. Cell nuclei were stained with DAPI. See Figures S42 and S43 for images of the individual channels.

precursor protein (APP) and the human P301L mutation of the 4R2N (Tau_{441}) isoform of the human tau protein, as well as a M146V mutated version of PSEN1, involved in the processing of APP to $A\beta_{1-42}$ peptides. The combined effect of these three mutations ensures the presence of both tau tangles and beta amyloid plaques by 12 and 6 months of age, respectively.

Two different methods were used to ascertain the pathology selectivity of **Tau 1**. Firstly, using hippocampal brain sections of 15-month-old mice, we identified a clear co-localization of **Tau 1** with the hysphorylated tau protein specific antibody AT180 upon tissue staining (Figure S42). The pyramidal neurons of the hippocampus demonstrated fluorescence originating from the somatodendritic compartments, both in the AT180 and **Tau 1** fluorescent windows, mirroring the findings of the primary literature of the 3xTg model.[43]

Beta amyloid plaques in these brain sections were identified with the pan-Aβ fluorescent antibody 6e10 and co-staining with **Tau 1** demonstrated a very weak signal from the plaque's core only (Figure S43). Comparing the co-localization in tau tangle rich sections and the Aβ plaques demonstrates the high selectivity of **Tau 1** for tau pathology over Aβ aggregates (Figure 7), confirming the results obtained in the solution and cell based assays (Figures 3 and 4).

Secondly, a 3xTg mouse was intracranially injected with **Tau 1**, to assess the *in vivo* distribution of the dye. After the mouse was sacrificed the hippocampal regions of the brain were co-stained with antibodies for hyperphosphorylated tau protein (AT180), Aβ plaques (sig 39200) and APP (mab348). As can be seen from Figures 8 and S44, **Tau 1** clearly co-localizes with tau pathology but not with Aβ pathology under these conditions as well.

***In vivo* imaging of Tau 1 in a transgenic mouse model of tauopathy.** As NIR emissive dyes allow for deep tissue penetration, we finally determined the *in vivo* imaging of **Tau 1** fluorescence in the Tau P301L mouse model as well as a wild-type mouse model. The P301L mouse

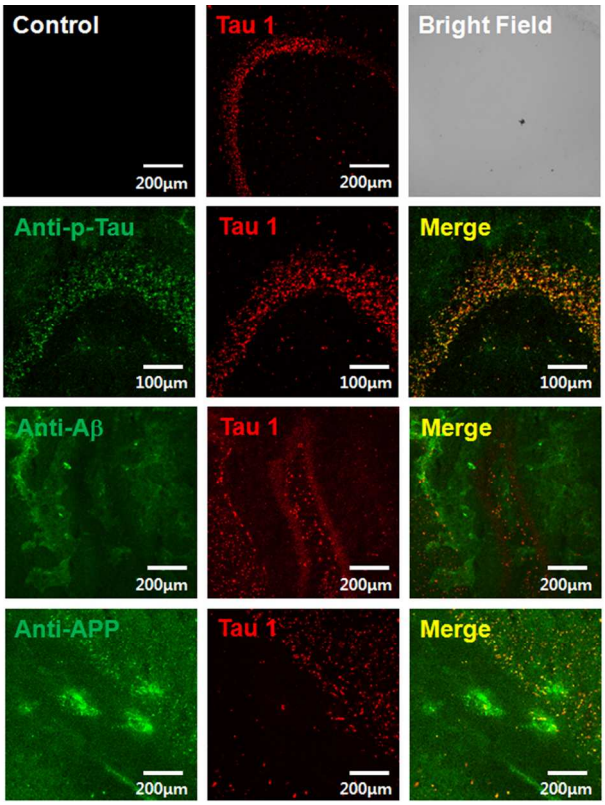

Figure 8. Confocal imaging of hippocampal regions of 3xTg mice intracranially injected with **Tau 1**. First row: Control. Second row: dual staining with the hyperphosphorylated tau protein antibody (AT180) and **Tau 1** reveals a very high degree of overlap. Third row: dual staining with an Aβ antibody (sig 39200) and **Tau 1** reveals virtually no overlap. Bottom row: dual staining with an APP antibody (mab348) and **Tau 1** reveals virtually no overlap. The fluorescence image of **Tau 1** was collected using excitation at 633 nm with a 650 nm longpass filter and that of the antibodies was obtained using excitation at 488 nm with a 505-550 nm bandpass filter.

model specifically overexpresses the 4R2N (Tau_{441}) isoform of the human tau protein, with the aggregation-prone P301L mutation.[44] As can be seen in Figure 9, 30 minutes subsequent to tail vein injection, a significantly increased fluorescence intensity could be observed in the transgenic mouse model, as compared to the wild type of negative control samples, clearly demonstrating the ability of **Tau 1** to report the presence of tau tangles in live mice.

CONCLUSIONS

Despite the lack of a clear pharmacophore, we hereby demonstrate the feasibility of a straightforward structural modification affording highly sensitive and selective probes for the molecular surface formed by self-assembled microtubule associated tau protein. As such, **Tau 1** and **Tau 2** clearly adhere to a hypothesis related to the push-pull chromophore's conjugation distance on protein aggregate specificity, as formulated for an entirely different class of fluorophores. The incorporation of an extra lipophilic surface via ring fusion was not found to play a significant role. The docking studies on the PHF6

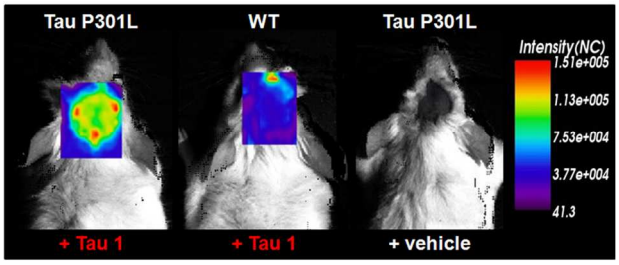

Figure 9. *In vivo* imaging of brains of Tau P301L mice or wild-type mice, 30 minutes subsequent to tail vein injection of **Tau 1** or vehicle. The fluorescence images were collected using excitation at 670 nm and the emission was monitored at 699 nm.

fragment of the R3 repeat of tau protein provide a potential binding mode of the dyes on the self-assembled tau protein, and could provide extra guidance in the design of novel tau binding molecules for imaging purposes. The probe is accessible via a short synthetic route and was found to exhibit excellent photophysical properties such as a large Stokes' shift as well as low cytotoxicity allowing *in vitro* and *ex vivo* imaging of hyperphosphorylated tau protein filaments with minimal background noise. The probes were clearly able to efficiently penetrate living cells to visualize the intracellular tau protein deposits. **Tau 1** also demonstrated efficient BBB penetration and displayed a high selectivity for tau tangles over Aβ deposits in transgenic mice models exhibiting both types of protein aggregates. Finally, **Tau 1** demonstrated the recognition of tau tangles in a transgenic mouse model *in vivo*, thus clearly showing the great potential of this dye for the discrimination of tau tangles in living organisms. Compared to a commercially available phosphorylated tau antibody, the probe performed exceptionally well, demonstrating a near perfect spatial overlap. Given the high monetary and time cost of synthesizing fluorescently labeled antibodies, the current fluorophore could represent a significant advantage over these antibodies for histological experiments. Furthermore, due to the efficient $^{18}F/^{19}F$ exchange at the boron center of BODIPY dyes, the current dye could also find applications as a dual NIR fluorescent and positron emission tomography imaging agent.

EXPERIMENTAL SECTION

Materials. All reactants and solvents were obtained from commercial suppliers (Sigma-Aldrich, Alfa, Samchun) and were used without further purification. THF was distilled over Na/benzophenone. $Aβ_{1-42}$ and AcPHF6 peptides were purchased from GenicBio Limited (Shanghai, China) and non-tagged 4R2N Tau_{441} was obtained through the MRC PPU Reagents and Services facility (MRC PPU, College of Life Sciences, University of Dundee, Scotland, mrcppureagents.dundee.ac.uk). NMR spectra were obtained on a 300 or 400 MHz Varian NMR spectrometer. UV/Vis spectra were recorded on a Scinco S-3100 spectrometer and fluorescence spectra were obtained using a Shimadzu RF-5301PC spectrofluorophotometer. Mass spectroscopy (ESI-MS) was per-

formed on a Shimadzu LCMS-2020 mass spectrometer system.

Spectroscopy in the presence of proteins. For spectroscopic measurements in the presence of proteins stock solutions of **ThT**, **Tau 1**, **Tau 2**, and **BAP-1** were prepared in DMSO. Both excitation and emission slit widths were 10 nm unless noted otherwise.

Quantum yields and determination of emission and fluorescence wavelength maxima. Data were recorded in HPLC grade solvents, with the absorbance lower than 0.1 at wavelengths longer or equal to the excitation wavelength to prevent the inner filter effect. The slit settings were 3 nm for both the excitation and the emission slits. The quantum yields of **BAP-1** and **Tau 1-2** were recorded *versus* Rhodamine B in 95% EtOH (Φ_{Fl} = 0.70),[45] using correction factors as previously described.[46]

Photostability. Solutions of **Rose Bengal**, **BAP-1** and **Tau 1-2** with an absorbance of 1.0 at the peak absorbance wavelength were prepared in DMF. The solutions were irradiated with the focused light of a 3300K halogen lamp using a Zeiss KL1500 LCD apparatus and the absorbance was determined in 5 minute intervals for 40 minutes. The photo-bleaching slopes of the BODIPY dyes were corrected for the spectral radiance of the lamp at the peak absorption wavelength relative to the spectral radiance of the lamp at the peak absorption wavelength of Rose Bengal.

DFT Calculations. Theoretical calculations using the density functional theory were performed using the B3LYP[47-50] functional at the 6-311++G** level of theory.[51-53] Calculations were carried out with the commercial Gaussian G09W software package.[54] Molecular orbitals were visualized using the Gabedit 2.4.8 software package.[55] Results are summarized in Table S1.

Docking studies. The optimized structures of **Tau 1**, **Tau 2**, **BAP-1**, **3h** and **PBB5** as well as the lead compounds in Table S2 were (re)calculated using the 6-31G* level of theory and were used as the input for the ligands, with the central boron atom of the BODIPY dyes replaced by a carbon, as parameters for the boron atom are not included in the docking software, as previously described for other BODIPY based probes.[56] For the docking studies on the isolated 6-mer PHF6, the molecular structure was constructed using the Avogadro 1.2.0 software package,[57] based on a X-ray crystal structure (PDB ID: 5K7N),[30] and the tunnel formed by 4 adjacent beta sheets forming a steric zipper along the fibril axis were constructed as a 5/6-mer from the same crystal structure similarly. The input files for the calculations were generated with the AutoDockTools 1.5.6 software package[58] and docking calculations were carried out using AutoDock Vina.[59] Visualization of the calculation results was performed using the Python Molecule Viewer 1.5.6 software package.[60]

Cell culture and fluorescent imaging. SH-SY5Y cells (human neuroblastoma) were grown in Dulbecco's Modified Eagle's Medium (DMEM), with 10% FBS (Gipco), penicillin (100 units/mL), and streptomycin (100 µg/mL). One day before imaging, the cells were placed on glass-bottomed dishes (SPL) which were incubated in a humidified atmosphere containing 5% (*v*/*v*) CO_2 at 37 °C. Cell images were obtained using a confocal microscope (Zeiss model LSM 510). All fluorescence images were obtained using an excitation wavelength of 458 nm (**ThT**), 633 nm (**Tau 1**, **Tau 2** and **BAP-1**) and a band pass emission filter at 475-525 nm (**ThT**), and a longpass (>650 nm) emission filter. Other information is available in the Figure captions.

Tau aggregation *in vitro*. Protein aggregation was performed in a 25 mM Tris buffer at pH 7, supplemented with 50 mM NaCl and 1 mM DTT Buffer, at 37 °C for 2hr to reduce any covalent tau dimers to monomers. The aggregation reaction was induced by heparin (2.5 µM).

Beta Amyloid aggregation. Beta Amyloid peptide (1-42) in the lyophilized form was dissolved at a concentration of 1.0 mg/ml in 100% HFIP (1,1,1,3,3,3-hexafluoro-2-propanol) and incubated at RT for 1 h. The solution was sonicated for 10 min and the solvent was removed by speed vac. The peptide was resuspended in DMSO as stock solution. Aliquots of 0.5 mM of this stock solution were diluted to 50 µM with 10 mM phosphate buffer (pH 7.4), containing 50 mM NaCl, 1.6 mM KCl, 2 mM $MgCl_2$ and 3.5 mM $CaCl_2$, prior to each experiment.

AcPHF6 aggregation inhibition assay. The assay was carried out analogous to literature procedures for 96 well plates[25,61] in a 10 mm fluorescent cuvette. Data are represented as the average of three measurements. Stock solutions used were as follows: (A) PBS (50 mM, pH 7.4), (B) 100 µM **BAP-1** or **Tau 1**in water with 0.5% DMSO, (C) 100 µM ThT in 50 mM PBS (50 mM, pH 7.4), (D) 1 mM AcPHF6 in pure H_2O. Each sample contained 1400 µL of solution A, 200 µL of solution B, 200 µL of solution C and 200 µL of solution D for a total solution of 2000 µL, controls were carried out as well. Solution D was added just prior to the start of the experiment. The fluorescence was measured for 30 minutes with data points each 0.16s with maximal stirring. Excitation and emission setting were 440/480 and 600/660 with slit width 3/3 and 10/10 to monitor the fluorescence of ThT or the NIR dyes, respectively. The data were corrected for the peptide precipitating from the solution, using an exponential decay correction after the initial rise in fluorescence intensity.

MTT assay. The MTT (3-(4,5-dimethylthiazol-2-yl)-2,5-diphenyltetrazolium bromide) assay was used to quantify cell viability. SH-SY5Y, SKNMC, U87, C6 and N2A cells 2×10^5/mL as well as human primary brain neurons (cat. 8800-10f, Cell Applications, San Diego, CA, USA) were treated with various concentrations of **Tau 1** and **Tau 2** in a 96-well plate for 48 h at 37°C. Then, an MTT solution of 5 mg/mL in serum free media was added to each well and cells were incubated for 1 h. Resulting formazan crystals were solubilized upon the addition of DMSO and the relative concentrations of formazan were determined by absorbance spectroscopy using a multi-well plate reader at 570 nm (*n*=3).

Acute animal model. 23 month-old or 10-week-old female wild-type C57BL/6 mice were anaesthetized with isoflurane vaporized in oxygen and 130 nL of 100 µM OA (Sigma Aldrich) solubilized in DMSO or DMSO alone was injected unilaterally to the lateral amygdala (n=3). At 24 h after the injection, 130 nL of 100 µM probe was applied at the injection site. Longitudinal sections containing the hippocampal CA1 and CA3 regions of interest were subjected to immunohistochemical labeling for the tau phospho-epitope AT180 (pTh231: Thermo Fisher). Prior to processing by paraffin embedding, brains were dissected into forebrain, hindbrain and cerebellum, as previously described.[34,62]

BBB penetration. ICR mice (male, 12-week-old) were used for the determination of the BBB permeability by using a modification of the in vivo mouse brain perfusion technique.[63-65] A solution of **Tau 1** (500 µM) in 20% DMSO

and 80% propylene glycol (100 µL) of was injected intravenously via the tail vein. After 1h, the mice were sacrificed, and the brains were removed from the skull and dissected on ice. The frozen brain was sliced into serial sections of 20 µm thickness. The fluorescence images of **Tau 1** were obtained using excitation at 633 nm with a 650 nm longpass filter using a confocal microscopy apparatus (LSM700, Carl Zeiss).

Determination of tau tangle selectivity of Tau 1. Tissue staining: 15-month-old female 3xTg mice[43] were sacrificed, and the brain was immediately removed and fixed for 24h in 4% formaldehyde. The brain was processed for paraffin embedding and sectioned at a thickness of 5 µm. The serial sections were dual stained with the hyper-phosphorylated tau protein antibody (AT180, Thermo Fisher) and **Tau 1**, and the amyloid beta antibody (6e10, Biolegend) and **Tau 1**, respectively. The fluorescence image of **Tau 1** was collected using excitation at 633 nm with a 650 nm longpass filter with a confocal microscope (LSM700, Carl Zeiss). The images of AT-180 and 6e10 were obtained using excitation at 488 nm with a 505-550 nm bandpass filter. Intracranial injection of **Tau 1**: analogous to the acute mouse model in a 17-month-old female 3xTg mice.[43] Longitudinal sections were stained with AT180 (Thermo Fisher), sig 39200 (BioLegend) mab348 (EMD Millipore). The fluorescence image of **Tau 1** was collected using excitation at 633 nm with a 650 nm longpass filter and that of AT180 was obtained using excitation at 488 nm with a 505-550 nm bandpass filter.

***In vivo* imaging.** Tau P301L mice (female, 12-month-old)[44] or ICR mice (female, 12-week-old) were injected with a solution of **Tau 1** (1 mM) in 30% DMSO/30% EtOH (50 µL) or 30% DMSO/30% EtOH (50 µL) alone *via* the tail vein. The mice were anesthetized with Zoletil 50 (Virbac, New Zealand) and *in vivo* fluorescence images of **Tau 1** and the negative control were collected using excitation at 670 nm and emission at 699 nm on an Optix MX3 Optical Molecular Imaging System (ART Advanced Research Technologies Inc., Canada).

Stereotaxic surgery. For histological sampling, mice were anaesthetized with a lethal dose of pentobarbitone followed by transcardial perfusion with 30 ml PBS, and subsequently 30 ml 4 % paraformaldehyde. Post-fixing of the brains, removed from the skull, was carried out overnight at 4 °C.

Immunocytochemistry. Serial sections were collected on gelatin-coated glass slides and air-dried in the dark. Without staining, glass coverslips were applied atop a fade retardant solution and mounted with cover slips for confocal observation. The brain sections were observed using a Carl Zeiss LSM 510 META laser-scanning microscope. The brain sections were fixed with 100% ethanol for 20 min and immunostained against the phospho-tau selective marker AT 180 or the $A\beta_{1\text{-}42}$ selective marker ab10148 (Abcam).

Western Blot. Tau protein phosphorylation after okadaic acid treatment: The SH-SY5Y cells were washed with PBS and subsequently homogenized through sonication in 50 mM Tris–HCl (pH 7.4), containing 150 mM NaCl, 0.5% Triton X-100, 1 mM EDTA, a protease inhibitor cocktail, and a phosphatase inhibitor cocktail (Sigma-Aldrich) for 30 min at 0°C. The homogenate was then centrifuged at 10,000 rpm for 15 min, resulting in a clear supernatant that was transferred into a new tube. After SDS-PAGE, the proteins were transferred onto a polyvinylidene difluoride membrane (Bio-Rad). The membrane was treated with in 3% BSA for overnight incubated with anti-tau (sc390476), anti-p-tau (sc101815), or anti-actin antibodies at 4°C. And the bands were visualized by super signal west femto (Thermo Fisher). Intracellular aggregation of $A\beta_{1\text{-}42}$: cell extracts of cells incubated with 50µg/mL $A\beta_{1\text{-}42}$ for 48 h, as well as a control, were run on a Tris-glycine gel (4-20%) as previously described in the literature.[35]

Synthesis of 1. 4,4-Difluoro-4-bora-3a,4a-diaza-*s*-indacene (**1**) was obtained using a reported procedure in 85% yield. Analytical data were in accordance with reported data in the literature.[66]

Synthesis of 4. 6-(Dimethylamino)-2-naphthaldehyde (**4**) was synthesized by a Bucherer-reaction according to a modified literature procedure.[67] In a 48 mL heavy walled glass pressure vessel (CAUTION: explosion risk, use protective equipment) 1.4 g (7.36 mmol) sodium metabisulfite and 800 mg (3.58 mmol) 6-bromo-2-naphthol was suspended in 8 mL water. To this stirred suspension, 2 mL 40 *wt*% aqueous dimethylamine (39 mmol) was added, and the reaction vessel was sealed and heated at 120°C for 60h. After the pressure vessel cooled down to room temperature, the reaction mixture was filtered. The solids were washed with water (3 × 20 mL) and the solids were dissolved in DCM. The organic layer was washed with water, and dried over Na_2SO_4. Column chromatography (silica, EtOAc/Hexane 8/1) yielded 505 mg (2.02 mmol, 56%) (6-bromo-2-naphthyl)dimethylamine as a white solid. Analytical data were in accordance with reported data in the literature.[67] To a solution of 900 mg (3.60 mmol) 6-bromo-2-naphthyl)amine in 9 mL anhydrous THF, 2.7 mL (a 1.6M solution) of *n*-BuLi in hexanes (4.32 mmol) were added at -78°C under inert atmosphere. The solution was stirred for 30 min, after which 2.7 mL anhydrous DMF was added dropwise. The solution was allowed to attain 0°C and is stirred at that temperature for another 2h, after which 15 mL of a saturated NH_4Cl solution in water was added. The resulting mixture was extracted with Et_2O (3 × 50 mL) and the organic layers were combined and dried over Na_2SO_4. Column chromatography (silica, EtOAc/Hexane 1/6) yielded 511 mg (2.56 mmol, 71%) of 6-(dimethylamino)-2-naphthaldehyde (**4**). Analytical data were in accordance with those reported in the literature.[67]

Synthesis of BAP-1. BAP-1 was synthesized via a Knoevenagel condensation following a literature procedure in a 50% yield.[18] Analytical data were in accordance with those reported in the literature.[18]

Synthesis of Tau 1. A solution of 100 mg (0.45 mmol) **1**, 84 mg (0.45 mmol) 4-(dimethylamino)cinnamaldehyde (**3**), 0.35 mL acetic acid and 0.35 mL piperidine in 10 mL toluene was heated under dean-stark conditions for 2h. The reaction was allowed to cool to room temperature and 50 mL of a saturated aqueous NH_4Cl solution was added. The mixture was extracted by EtOAc (3 × 50 mL) and the organic layers were combined and dried over Na_2SO_4. Column chromatography (silica, EtOAc/Hexane 1/20 →1/5) resulted in 22 mg (0.06 mmol, 13%) **Tau 1**. ^{1}H NMR (300 MHz, $CDCl_3$): δ 7.61 (s, 1H), 7.39 (d, J = 8.5 Hz, 2H), 7.29 – 7.16 (m, 1H), 7.13 – 6.99 (m, 2H), 6.99 – 6.78 (m, 3H), 6.75 – 6.62 (m, 3H), 6.45 – 6.36 (m, 1H), 3.03 (s, 6H), 2.28 (s, 3H) ppm. ^{13}C NMR (100 MHz, $CDCl_3$): δ 159.82, 151.22, 144.43, 142.92, 140.62, 138.75, 137.34, 133.12, 129.17, 124.74, 124.69, 124.41, 121.17, 119.73, 117.87, 115.85, 112.33, 40.44, 11.68 ppm. MS(ESI): $C_{22}H_{22}BF_2N_3$ $[M]^{\bullet+}$, m/z Calculated: 377.19, Found: 377.35.

Synthesis of Tau 2. A solution of 120 mg (0.55 mmol) **1**, 164 mg (0.83 mmol) **4**, 0.35 mL acetic acid and 0.35 mL piperi-

dine in 10 mL toluene was heated under dean-stark conditions for 2h. The reaction was allowed to cool to room temperature and 50 mL saturated aqueous NH_4Cl solution was added. The mixture was extracted by EtOAc (3 × 50 mL), the organic layers were combined and dried over Na_2SO_4. Column chromatography (silica, EtOAc/Hexane 1/15 →1/10) resulted in 70 mg (0.17 mmol, 32%) **Tau 2**. ^{1}H NMR (300 MHz, $CDCl_3$): δ 7.81 (s, 1H), 7.74 – 7.59 (m, 5H), 7.54 – 7.45 (m, 1H), 7.13 (dd, J = 9.2 Hz, J = 2.4 Hz, 1H) 7.10 (s, 1H), 6.90 – 6.84 (m, 2H), 6.79 (s, 1H), 6.47 – 6.41 (m, 1H), 3.10 (s, 6H), 2.31 (s, 3H) ppm. ^{13}C NMR (100 MHz, $CDCl_3$): δ 159.98, 149.73, 144.71, 141.76, 138.46, 137.78, 136.37, 133.12, 130.01, 130.00, 129.70, 127.05, 126.38, 124.93, 124.66,121.97, 117.65, 116.47, 116.45, 116.07, 106.17, 40.76, 11.72 ppm. MS(ESI): $C_{24}H_{22}BF_2N_3$ $[M+H]^+$, m/z Calculated: 402.19, Found: 402.35; $[2M+H]^+$ m/z Calculated: 803.38, Found: 803.50.

■ ASSOCIATED CONTENT

Supporting Information. ^{1}H and ^{13}C NMR and ESI-MS data of new compounds, absorption and emission spectra, DFT calculation details, supporting solution experiments, probe toxicity, Western blotting of OA treated cells and supporting tissue staining results. This material is available free of charge via the Internet at http://pubs.acs.org.

■ AUTHOR INFORMATION

Corresponding Author

* shinarago@khu.ac.kr (J-WS)
* jhkwak@skku.edu (JHK)
* kangch@khu.ac.kr (CK)
* jongskim@korea.ac.kr (JSK)

Author Contributions

‡ These authors contributed equally.

Notes

The authors declare no competing financial interest.

■ ACKNOWLEDGMENTS

This work was supported by the Ministry of Science, ICT & Future Planning (MSIP) of National Research Foundation of Korea (No. 2009-0081566, JSK), the Korea Research Fellowship Program funded by the Ministry of Science, ICT and Future Planning through the National Research Foundation of Korea (2016H1D3A1938052, PV), a Korean Health Technology R&D project (HI16C1010, CK), funded by the Korean Ministry of Health &Welfare, and a healthy aging project grant (20151022, J-WS) from the Korea Health Industry Development Institute, Republic of Korea.

■ REFERENCES

(1) Crowther, R. A. *Proc. Natl. Acad. Sci. U. S. A.* **1991**, *88*, 2288-2292.

(2) Ittner, L. M.; Götz, J. *Nat. Rev. Neurosci.* **2011**, *12*, 67-72.

(3) Spillantini, M. G.; Goedert, M. *Lancet Neurol.* **2013**, *12*, 609-622.

(4) Arriagada, P. V.; Growdon, J. H.; Hedley-whyte, E. T.; Hyman, B. T. *Neurology* **1992**, *42*, 631-639.

(5) Buée, L.; Bussière, T.; Buée-Scherrer, V.; Delacourte, A.; Hof, P. R. *Brain Res. Brain Res. Rev.* **2000**, *33*, 95-130.

(6) Morris, M.; Maeda, S.; Vossel, K.; Mucke, L. *Neuron* **2011**, *70*, 410-426.

(7) del Carmen Cárdenas-Aguayo, M.; Gómez-Virgilio, L.; DeRosa, S.; Meraz-Ríos, M. A. *ACS Chem. Neurosci.* **2014**, *5*, 1178-1191.

(8) Martin, L.; Latypova, X.; Terro, F. *Neurochem. Int.* **2011**, *58*, 458-471.

(9) Cohen, T. J.; Guo, J. L.; Hurtado, D. E.; Kwong, L. K.; Mills, I. P.; Trojanowski, J. Q.; Lee, V. M. Y. *Nat. Commun.* **2011**, *2*, 252.

(10) Funk, K. E.; Thomas, S. N.; Schafer, K. N.; Cooper, G. L.; Liao, Z.; Clark, D. J.; Yang, A. J.; Kuret, J. *Biochem. J* **2014**, *462*, 77-88.

(11) Khan, S. S.; Bloom, G. S. *Front. Neurosci.* **2016**, *10*, 31.

(12) Zempel, H.; Mandelkow, E. *Trends Neurosci.* **2014**, *37*, 721-732.

(13) Wegmann, S.; Medalsy, I. D.; Mandelkow, E.; Müller, D. J. *Proc. Natl. Acad. Sci. U. S. A.* **2013**, *110*, E313-E321.

(14) Ariza, M.; Kolb, H. C.; Moechars, D.; Rombouts, F.; Andrés, J. I. *J. Med. Chem.* **2015**, *58*, 4365-4382.

(15) Maruyama, M.; Shimada, H.; Suhara, T.; Shinotoh, H.; Ji, B.; Maeda, J.; Zhang, M.-R.; Trojanowski, J. Q.; Lee, V. M.-Y.; Ono, M.; Masamoto, K.; Takano, H.; Sahara, N.; Iwata, N.; Okamura, N.; Furumoto, S.; Kudo, Y.; Chang, Q.; Saido, T. C.; Takashima, A.; Lewis, J.; Jang, M.-K.; Aoki, I.; Ito, H.; Higuchi, M. *Neuron* **2013**, *79*, 1094-1108.

(16) Ojida, A.; Sakamoto, T.; Inoue, M.-a.; Fujishima, S.-h.; Lippens, G.; Hamachi, I. *J. Am. Chem. Soc.* **2009**, *131*, 6543-6548.

(17) Seo, Y.; Park, K.-s.; Ha, T.; Kim, M. K.; Hwang, Y. J.; Lee, J.; Ryu, H.; Choo, H.; Chong, Y. *ACS Chem. Neurosci.* **2016**, *7*, 1474-1481.

(18) Ono, M.; Watanabe, H.; Kimura, H.; Saji, H. *ACS Chem. Neurosci.* **2012**, *3*, 319-324.

(19) Loudet, A.; Burgess, K. *Chem. Rev.* **2007**, *107*, 4891-4932.

(20) Boens, N.; Leen, V.; Dehaen, W. *Chem. Soc. Rev.* **2012**, *41*, 1130-1172.

(21) Catalàn, J. *J. Phys. Chem. B* **2009**, *113*, 5951-5960.

(22) von Bergen, M.; Friedhoff, P.; Biernat, J.; Heberle, J.; Mandelkow, E. M.; Mandelkow, E. *Proc. Natl. Acad. Sci. U.S.A.* **2000**, *97*, 5129-5134.

(23) Ganguly, P.; Do, T. D.; Larini, L.; LaPointe, N. E.; Sercel, A. J.; Shade, M. F.; Feinstein, S. C.; Bowers, M. T.; Shea, J.-E. *J. Phys. Chem. B* **2015**, *119*, 4582-4593.

(24) Sievers, S.A.; Karanicolas, J.; Chang, H. W.; Zhao, A.; Jiang, L.; Zirafi, O.; Stevens, J. T.; Münch, J.; Baker, D.; Eisenberg, D. *Nature*, **2011**, *475*, 96-100.

(25) Zheng, J.; Liu, C.; Sawaya, M. R.; Vadla, B.; Khan, S.; Woods, R. J.; Eisenberg, D.; Goux, W.J.; Nowick, J. S. *J. Am. Chem. Soc.* **2011**, *133*, 3144-3157.

(26) Bulic, B.; Pickhardt, M.; Mandelkow, E. M.; Mandelkow, E. *Neuropharmacol.* **2010**, *59*, 276-289.

(27) Sawaya, M. R.; Sambashivan, S.; Nelson, R.; Ivanova, M. I.; Sievers, S. A.; Apostol, M. I.; Thompson, M. J.; Balbirnie, M.; Wiltzius, J. J.; McFarlane, H. T.; Madsen, A. Ø.; Riekel, C.; Eisenberg, D. *Nature* **2007**, *447*, 453-457.

(28) Landau, M.; Sawaya, M. R., Faull, K. F.; Laganowsky, A.; Jiang, L.; Sievers, S. A.; Liu, J.; Barrio, J. R.; Eisenberg, D. *Plos Biol.* **2011**, 9, e1001080.

(29) Wiltzius, J. J.; Landau, M.; Nelson, R.; Sawaya, M. R.; Apostol, M. I.; Goldschmidt, L.; Soriaga, A. B.; Cascio, D.; Rajashankar, K.; Eisenberg, D. *Nat. Struct. Mol. Biol.* **2009**, *16*, 973-978.

(30) de la Cruz, M. J.; Hattne, J.; Shi, D.; Seidler, P.; Rodriguez, J.; Reyes, F. E.; Sawaya, M. R.; Cascio, D.; Weiss, S. C.; Kim, S. K.; Hinck, C. S.; Hinck, A. P.; Calero, G.; Eisenberg, D.; Gonen, T. *Nat. Methods* **2017**, *14*, 399-402.

(31) Groenning, M.; Olsen, L.; van de Weert, M.; Flink, J. M.; Frokjaer, S.; Jørgensen, F. S. *J. Struct. Biol.* **2007**, *158*, 358-369.

(32) Goedert, M.; Jakes, R.; Spillantini, M. G.; Hasegawa, M.; Smith, M. J.; Crowther, R. A. *Nature* **1996**, *383*, 550-553.
(33) Zhang, Z.; Simpkins, J. W. *Brain Res.* **2010**, *1345*, 176-181.
(34) Baker, S.; Götz, J. *Acta Neuropathol. Commun.* **2016**, *4*, 32.
(35) Hu, X.; Crick, S. L.; Bu, G.; Frieden, C.; Pappu, R. V.; Lee, J.-M. *Proc. Natl. Acad. Sci.* **2009**, *106*, 20324-20329.
(36) Wesén, E.; Jeffries, G. D. M.; Matson Dzebo, M.; Esbjörner, E. K. *Sci. Rep.* **2017**, *7*, 2021.
(37) de Calignon, A.; Polydoro, M.; Suárez-Calvet, M.; William, C.; Adamowicz, D. H.; Kopeikina, K. J.; Pitstick, R.; Sahara, N.; Ashe, K. H.; Carlson, G. A.; Spires-Jones, T. L.; Hyman, B. T. *Neuron* **2012**, *73*, 685-697.
(38) Schindelin, J.; Rueden, C. T.; Hiner, M. C.; Eliceiri, K. W. *Mol. Reprod. Dev.* **2015**, *82*, 518-529.
(39) Braak, H.; Braak, E. *Acta Neuropathol.* **1991**, *82*, 239-259.
(40) Veeranna; Yang, D.-S.; Lee, J.-H.; Vinod, K. Y.; Stavrides, P.; Amin, N. D.; Pant, H. C.; Nixon, R. A. *Neurobiol. Aging* **2011**, *32*, 2016-2029.
(41) Qian, W.; Shi, J.; Yin, X.; Iqbal, K.; Grundke-Iqbal, I.; Gong, C.-X.; Liu, F. *J. Alzheimers Dis.* **2010**, *19*, 1221-1229.
(42) Haystead, T. A. J.; Sim, A. T. R.; Carling, D.; Honnor, R. C.; Tsukitani, Y.; Cohen, P.; Hardie, D. G., *Nature* **1989**, *337*, 78-81.
(43) Oddo, S.; Caccamo, A.; Shepherd, J. D.; Murphy, M. P.; Golde, T. E.; Kayed, R.; Metherate, R.; Mattson, M. P.; Akbari, Y.; LaFerla, F. M. *Neuron* **2003**, *39*, 409-421.
(44) Terwel, D.; Lasrado, R.; Snauwaert, J,; Vandeweert, E.; Van Haesendonck, C.; Borghgraef, P.; Van Leuven, F. *J. Biol. Chem.* **2005**, *280*, 3963-3973.
(45) Arbeloa, F. L.; Ojeda, P. R.; Arbeloa, I. L. *J. Lumin.* **1989**, *44*, 105-112.
(46) Brouwer, A. M. *Pure Appl. Chem.* **2011**, *83*, 2213-2228.
(47) Vosko, S. H.; Wilk, L.; Nusair, M. *Can. J. Phys.* **1980**, *58*, 1200-1211.
(48) Lee, C. T.; Yang, W. T.; Parr, R. G. *Phys. Rev. B* **1988**, *37*, 785-789.
(49) Becke, A. D. *J. Chem. Phys.* **1993**, *98*, 5648-5652.
(50) Stephens, P. J.; Devlin, F. J.; Chabalowski, C. F.; Frisch, M. J. *J. Phys. Chem.* **1994**, *98*, 11623-11627.
(51) Krishnan, R.; Binkley, J. S.; Seeger, R.; Pople, J. A. *J. Chem. Phys.* **1980**, *72*, 650-654.
(52) McLean, A. D.; Chandler, G. S. *J. Chem. Phys.* **1980**, *72*, 5639-5648.
(53) Clark, T.; Chandrasekhar, J.; Spitznagel, G. W.; Schleyer, P. V. R. *J. Comput. Chem.* **1983**, *4*, 294-301.
(54) Frisch, M. J.; Trucks, G. W.; Schlegel, H. B.; Scuseria, G. E.; Robb, M. A.; Cheeseman, J. R.; Scalmani, G.; Barone, V.; Mennucci, B.; Petersson, G. A.; Nakatsuji, H.; Caricato, M.; Li, X.; Hratchian, H. P.; Izmaylov, A. F.; Bloino, J.; Zheng, G.; Sonnenberg, J. L.; Hada, M.; Ehara, M.; Toyota, K.; Fukuda, R.; Hasegawa, J.; Ishida, M.; Nakajima, T.; Honda, Y.; Kitao, O.; Nakai, H.; Vreven, T.; Montgomery Jr., J. A.; Peralta, J. E.; Ogliaro, F.; Bearpark, M. J.; Heyd, J.; Brothers, E. N.; Kudin, K. N.; Staroverov, V. N.; Kobayashi, R.; Normand, J.; Raghavachari, K.; Rendell, A. P.; Burant, J. C.; Iyengar, S. S.; Tomasi, J.; Cossi, M.; Rega, N.; Millam, N. J.; Klene, M.; Knox, J. E.; Cross, J. B.; Bakken, V.; Adamo, C.; Jaramillo, J.; Gomperts, R.; Stratmann, R. E.; Yazyev, O.; Austin, A. J.; Cammi, R.; Pomelli, C.; Ochterski, J. W.; Martin, R. L.; Morokuma, K.; Zakrzewski, V. G.; Voth, G. A.; Salvador, P.; Dannenberg, J. J.; Dapprich, S.; Daniels, A. D.; Farkas, Ö.; Foresman, J. B.; Ortiz, J. V.; Cioslowski, J.; Fox, D. J.; Gaussian, Inc.: Wallingford, CT, USA, 2010.
(55) Allouche, A.-R. *J. Comput. Chem.* **2011**, *32*, 174-182.
(56) Teoh, C. L.; Su, D.; Sahu, S.; Yun, S.-W.; Drummond, E.; Prelli, F.; Lim, S.; Cho, S.; Ham, S.; Wisniewski, T.; Chang, Y.-T. *J. Am. Chem. Soc.* **2015**, *137*, 13503-13509.
(57) Hanwell, M. D.; Curtis, D. E.; Lonie, D. C.; Vandermeersch, T.; Zurek, E.; Hutchison, G. R. *J. Cheminform.* **2012**, *4*, 17.
(58) Morris, G. M.; Huey, R.; Lindstrom, W.; Sanner, M. F.; Belew, R. K.; Goodsell, D. S.; Olson, A. J. *J. Comput. Chem.* **2009**, *30*, 2785-2791.
(59) Trott, O.; Olson, A. J. *J. Comput. Chem.* **2010**, *31*, 455-461.
(60) Sanner, M. F. *J. Mol. Graphics Modell.* **1999**, *17*, 57-61.
(61) Lunven, L.; Bonnet, H.; Yahiaoui, S.; Yi, W.; Da Costa, L.; Peuchmaur, M.; Boumendjel, A.; Chierici, S. *ACS Chem. Neurosci.* **2016**, *7*, 995-1003.
(62) Lee, Y. O.; Shin, J.-W.; Yi, C.; Lee, Y. H.; Sohn, N.-W.; Kang, C.; Kim, J. S. *Chem. Commun.* **2014**, *50*, 5741-5744.
(63) Dagenais, C.; Rousselle, C.; Pollack, G. M.; Scherrmann, I.-M. *J. Cerebr. Blood F. Met.* **2000**, *20*, 381-386.
(64) Murakami, H.; Takanaga, H.; Matsuo, H.; Ohtani, H.; Sawada, Y. *Am. J. Physiol. Heart Circ. Physiol.* **2000**, *279*, H1022-H1028.
(65) Ujiie, M.; Dickstein, D. L.; Carlow, D. A.; Jefferies, W. A. *Microcirculation* **2003**, *10*, 463-470
(66) Lee, J.-S.; Kang, N.-y.; Kim, Y. K.; Samanta, A.; Feng, S.; Kim, H. K.; Vendrell, M.; Park, J. H.; Chang, Y.-T. *J. Am. Chem. Soc.* **2009**, *131*, 10077-10082.
(67) Petrič, A.; Johnson, S. A.; Pham, H. V.; Li, Y.; Čeh, S.; Golobič, A.; Agdeppa, E. D.; Timbol, G.; Liu, J.; Keum, G.; Satyamurthy, N.; Kepe, V.; Houk, K. N.; Barrio, J. R. *Proc. Natl. Acad. Sci. U. S. A.* **2012**, *109*, 16492-16497.

Table of Contents (TOC)

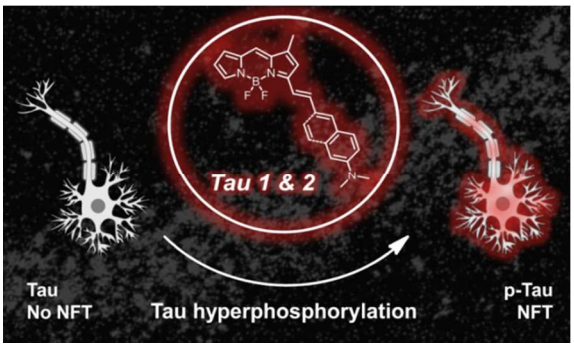

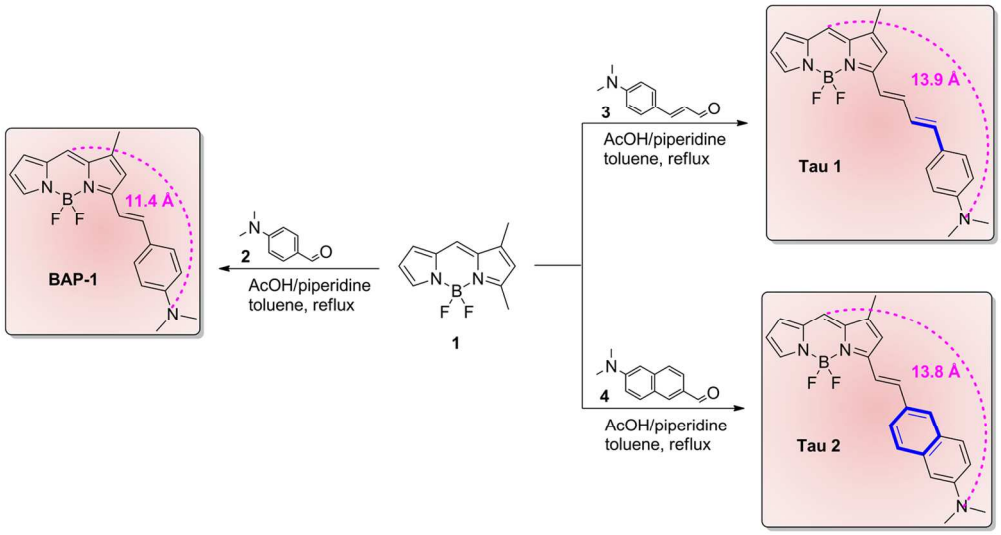

Scheme 1. Synthetic approach towards BAP-1 and Tau 1-2. The structural modifications relative to BAP-1 are marked in blue. The N - BODIPY C8 (meso) distance, as determined from the optimized structure by DFT is shown in magenta (See SI for DFT calculation details).

133x71mm (300 x 300 DPI)

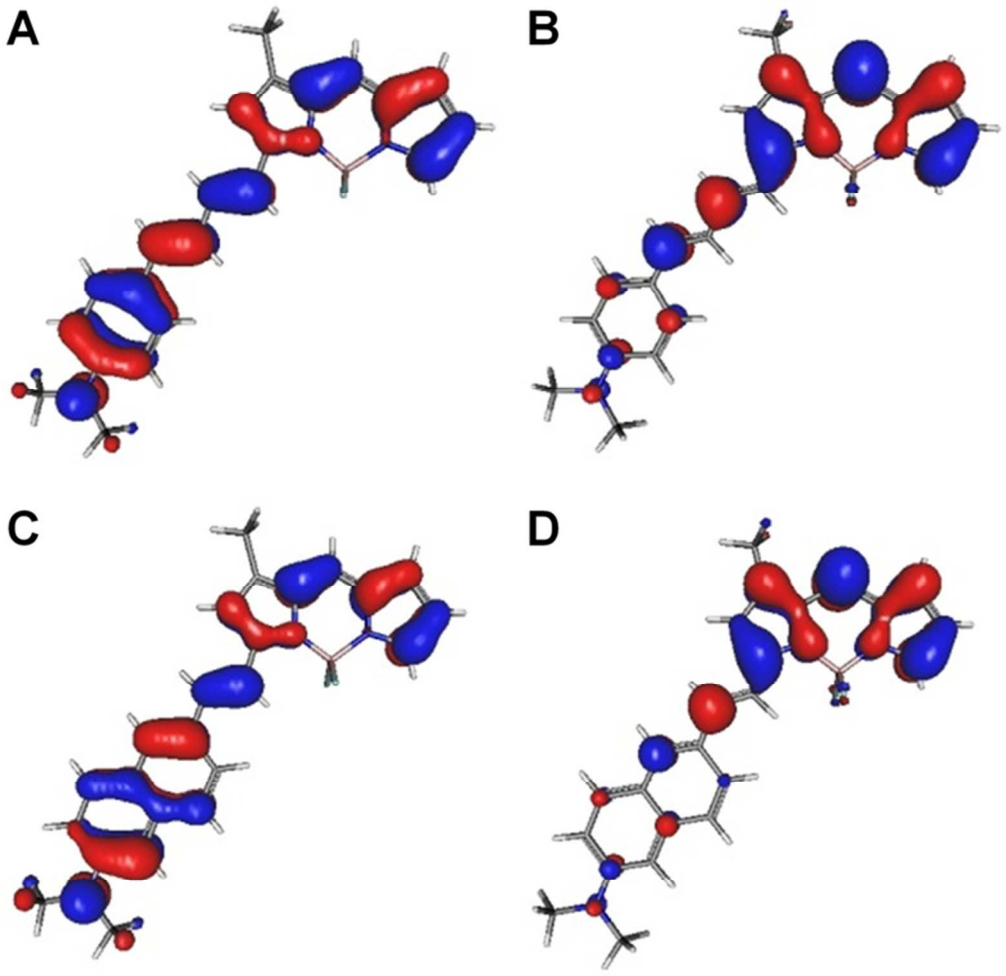

Figure 1. Calculated frontier orbitals of Tau 1 and Tau 2 by density functional theory using B3LYP at the 6-311++G** level of theory. (a-b) HOMO and LUMO orbital of Tau 1. (c-d) HOMO and LUMO orbital of Tau 2. Electron densities are displayed at the 0.03 e·bohr-3 isodensity surface.

66x65mm (300 x 300 DPI)

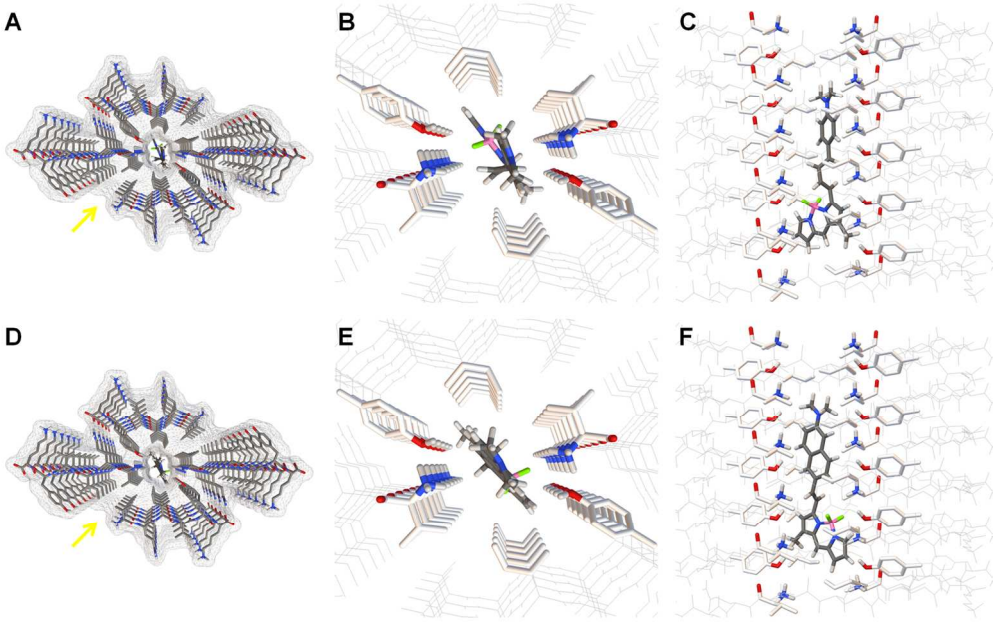

Figure 2. Molecular docking of Tau 1 (A-C) and Tau 2 (D-F). A and D) Top view of the molecule docked in the tunnel formed by 4 adjacent stacked beta sheets, protein molecular surface depicted. B and E) zoomed top view of the tunnel, side chains comprising the tunnel are depicted as sticks, others as lines. C and F) Side view of the molecule in the in the protein tunnel, side chains comprising the tunnel are depicted as sticks, others as lines. The yellow arrow indicates the viewing direction for panels C and F

148x94mm (300 x 300 DPI)

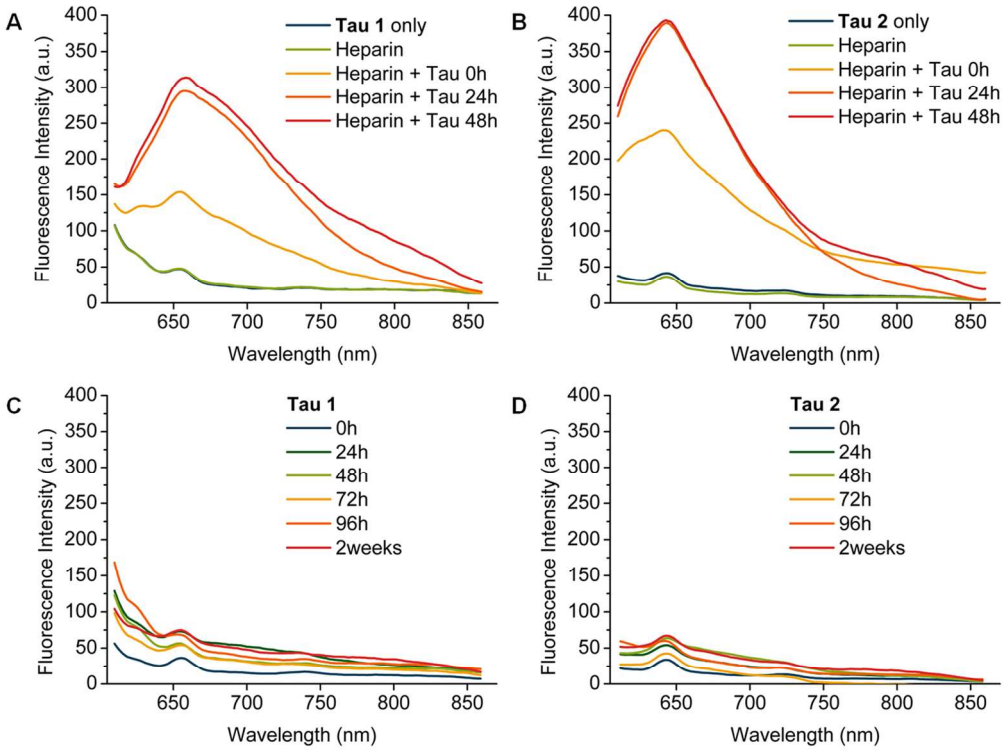

Figure 3. Time dependent fluorescence enhancement of Tau 1-2 (10 μM) in the presence of protein aggregates. (a) Emission spectra of Tau 1 in the presence of tau protein (10 μM) and heparin (2.5 μM), excited at 590 nm, (b) Emission spectra of Tau 1 in the presence of tau protein (10 μM) and heparin (2.5 μM), excited at 580 nm, (C-D) Emission spectra of Tau 1-2 in the pres-ence of Aβ fibrils (50 μM).

140x108mm (300 x 300 DPI)

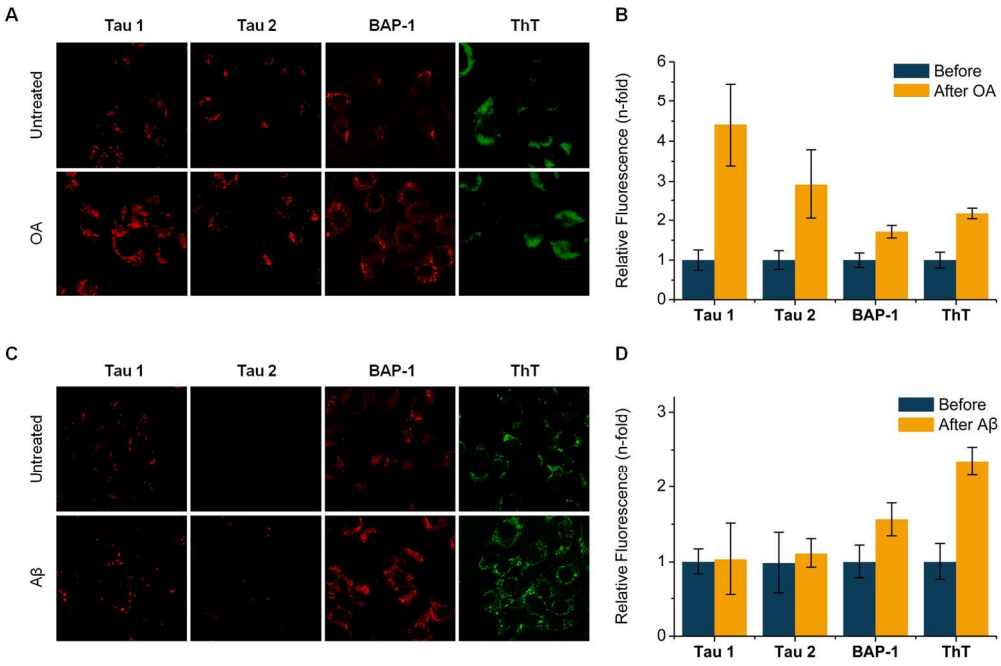

Figure 4. (a) Fluorescence images of SH-SY5Y cells incubated with Tau 1, Tau 2, BAP-1 and ThT (500 nM) for 20 min at 37°C. Top: Untreated cells, Bottom: pre-incubated with okadaic acid (100 nM) for 6hr. ThT was excited at 458 nm and the emission was recorded using a 475-525 nm band pass filter. Tau 1-2 and BAP-1 were excited at 633 nm and the fluorescence was collected at wavelengths higher than 650 nm. (b) Florescence intensity per cell relative to untreated cells (n=5), as determined using image J.38 Error bars designate standard deviation. (c) Fluorescence images of SH-SY5Y cells using amyloid beta peptide with Tau 1, Tau 2, BAP-1 and ThT. After treatment of amyloid beta peptide (50 µg/mL) for 48 hr, the probes (1 µM) were incubation for 15 min at 37°C (bottom). Untreated cells were incubated with the probes for 15 min without peptide (top). ThT was excited at 458 nm and the emission was recorded using a 475-525 nm band pass filter, Tau 1-2 and BAP-1 were excited at 633 nm and the fluorescence was collected at wavelengths higher than 650 nm. (d) Fluorescence intensity per cell relative to untreated cells (n=5), as determined using image J.38 Error bars designate standard deviation.

170x111mm (300 x 300 DPI)

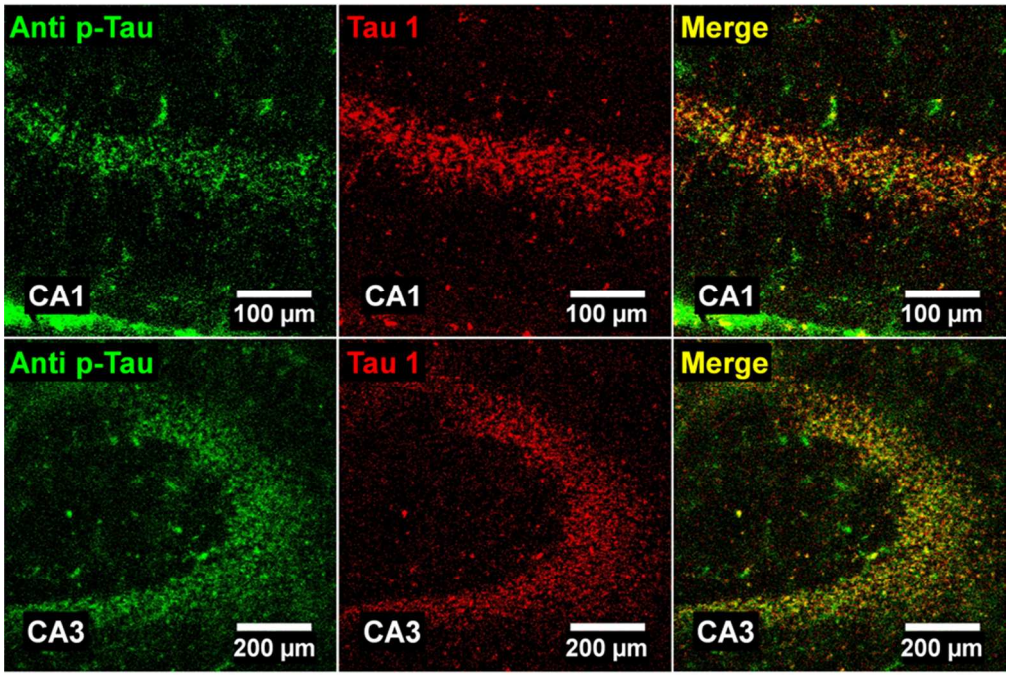

Figure 5. Confocal imaging of the CA1 (Top) and CA3 (Bottom) hippocampal regions of OA treated mice. Dual staining with the hyperphosphorylated tau protein antibody (AT-180) and Tau 1 reveals a very high degree of overlap. The fluorescence image of Tau 1 was collected using excitation at 633 obtained using excitation at 488 nm with a 505-550 nm bandpass filter.

81x54mm (300 x 300 DPI)

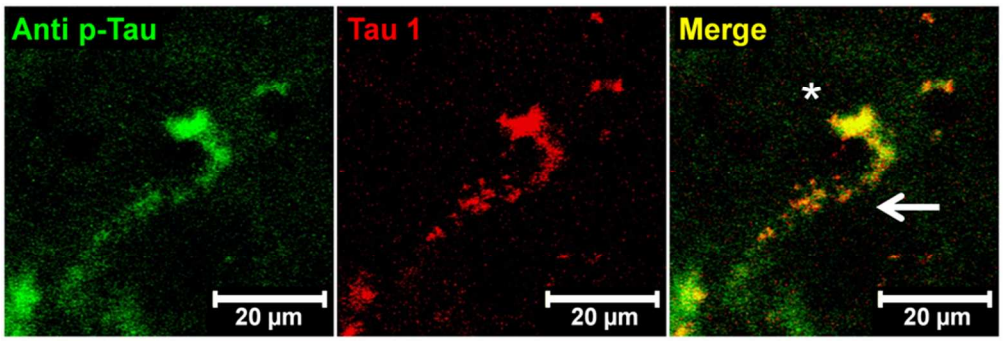

Figure 6. Confocal imaging of a single hippocampal neuron of an OA treated mouse. Dual staining with the hyperphosphorylated tau protein antibody AT-180 and Tau 1 demonstrates significant amounts of tau missorting to the somatodendritic compartment (*) of the neuron, as well as sporadic hyperphosphorylated tau deposits along the axon (arrow). The fluorescence image of Tau 1 was collected using excitation at 633 nm with a 650 nm longpass filter and that of AT180 was obtained using excitation at 488 nm with a 505-550 nm bandpass filter.

81x27mm (300 x 300 DPI)

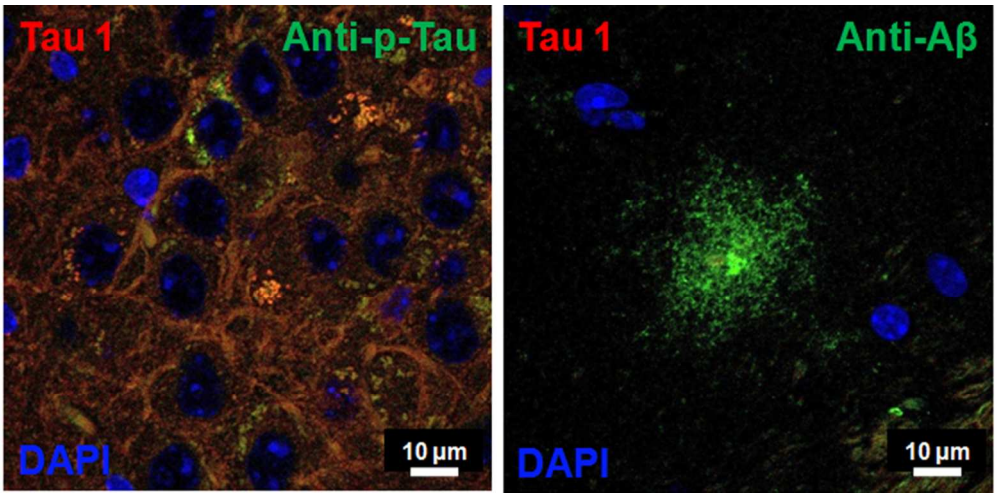

Figure 7. Merged confocal imaging of hippocampal regions of 3xTg mice. Left: Dual staining with the hyperphosphorylated tau protein antibody AT180 and Tau 1; Right: Dual staining with the amyloid beta antibody 6e10 and Tau 1. The fluorescent image of Tau 1 was obtained using excitation at 633 nm with a 650 nm longpass filter and AT180 and 6e10 were obtained using excitation at 488 nm with a 505-550 nm bandpass filter. Cell nuclei were stained with DAPI. See Figures S42 and S43 for images of the individual channels.

82x39mm (300 x 300 DPI)

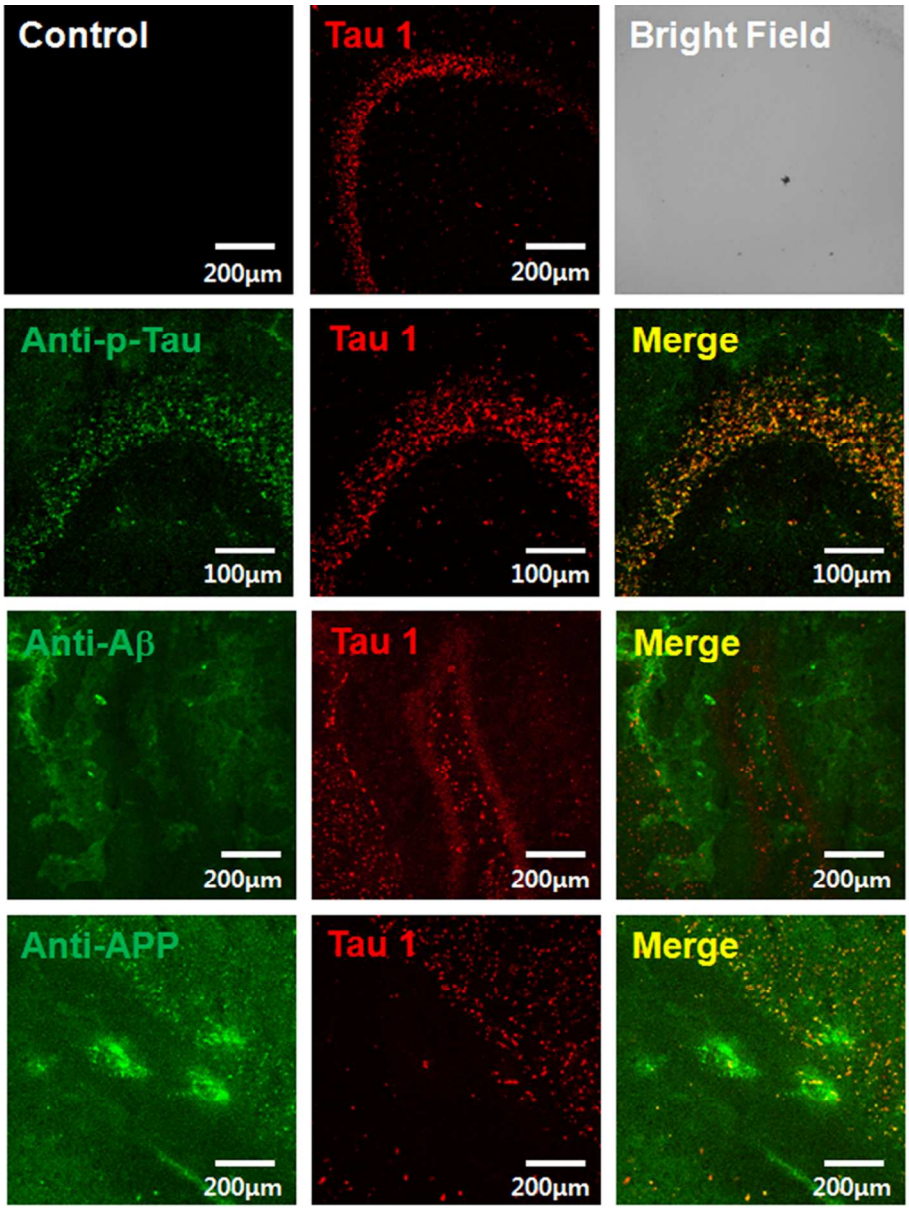

Figure 8. Confocal imaging of hippocampal regions of 3xTg mice intracranially injected with Tau 1. First row: Control. Second row: dual staining with the hyperphosphorylated tau protein antibody (AT180) and Tau 1 reveals a very high de-gree of overlap. Third row: dual staining with an Aβ anti-body (sig 39200) and Tau 1 reveals virtually no overlap. Bottom row: dual staining with an APP antibody (mab348) and Tau 1 reveals virtually no overlap. The fluorescence image of Tau 1 was collected using excitation at 633 nm with a 650 nm longpass filter and that of the antibodies was ob-tained using excitation at 488 nm with a 505-550 nm band-pass filter.

80x105mm (300 x 300 DPI)

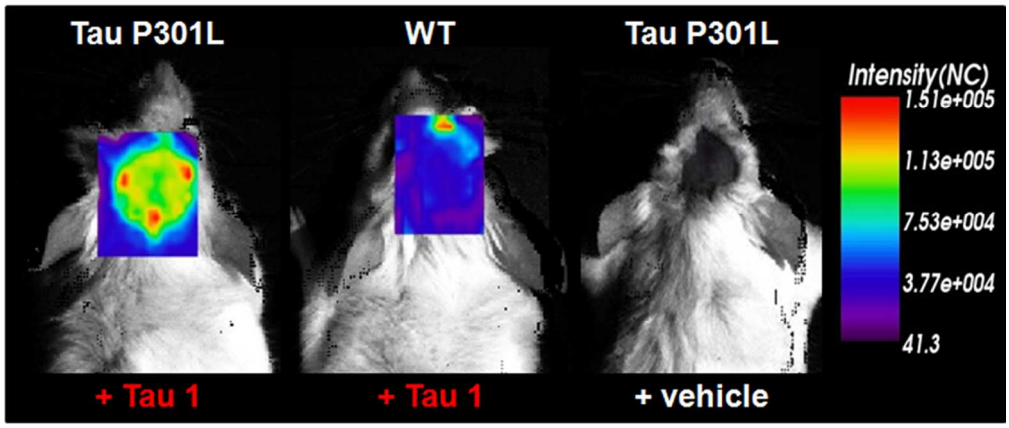

Figure 9. In vivo imaging of brains of Tau P301L mice or wild-type mice, 30 minutes subsequent to tail vein injection of Tau 1 or vehicle. The fluorescence images were collected using excitation at 670 nm and the emission was monitored at 699 nm.

82x34mm (300 x 300 DPI)